materials

MDPI

Review

Structural Phase Transition and In-Situ Energy Storage Pathway in Nonpolar Materials: A Review

Xian-Kui Wei [1,*], Rafal E. Dunin-Borkowski [1] and Joachim Mayer [1,2]

[1] Ernst Ruska-Centre for Microscopy and Spectroscopy with Electrons, Research Centre Jülich, 52425 Jülich, Germany; rdb@fz-juelich.de (R.E.D.-B.); mayer@gfe.rwth-aachen.de (J.M.)
[2] Gemeinschaftslabor für Elektronenmikroskopie (GFE), RWTH Aachen University, 52074 Aachen, Germany
* Correspondence: x.wei@fz-juelich.de

Abstract: Benefitting from exceptional energy storage performance, dielectric-based capacitors are playing increasingly important roles in advanced electronics and high-power electrical systems. Nevertheless, a series of unresolved structural puzzles represent obstacles to further improving the energy storage performance. Compared with ferroelectrics and linear dielectrics, antiferroelectric materials have unique advantages in unlocking these puzzles due to the inherent coupling of structural transitions with the energy storage process. In this review, we summarize the most recent studies about in-situ structural phase transitions in $PbZrO_3$-based and $NaNbO_3$-based systems. In the context of the ultrahigh energy storage density of $SrTiO_3$-based capacitors, we highlight the necessity of extending the concept of antiferroelectric-to-ferroelectric (AFE-to-FE) transition to broader antiferrodistortive-to-ferrodistortive (AFD-to-FD) transition for materials that are simultaneously ferroelastic. Combining discussion of the factors driving ferroelectricity, electric-field-driven metal-to-insulator transition in a $(La_{1-x}Sr_x)MnO_3$ electrode is emphasized to determine the role of ionic migration in improving the storage performance. We believe that this review, aiming at depicting a clearer structure–property relationship, will be of benefit for researchers who wish to carry out cutting-edge structure and energy storage exploration.

Keywords: energy storage; in situ; antiferrodistortive-to-ferrodistortive; phase transition; metal-to-insulator transition; ionic migration

Citation: Wei, X.-K.; Dunin-Borkowski, R.E.; Mayer, J. Structural Phase Transition and In-Situ Energy Storage Pathway in Nonpolar Materials: A Review. *Materials* **2021**, *14*, 7854. https://doi.org/10.3390/ma14247854

Academic Editors: Zibin Chen, Xiaozhou Liao and Wenge Yang

Received: 9 November 2021
Accepted: 16 December 2021
Published: 18 December 2021

1. Introduction

Renewable energies harvested from solar, wind and chemical fuels are playing ever-greater roles in our lives [1,2]. However, their widespread utilization is largely impeded by the underdeveloped energy storage technologies. Thus far, popular electrical energy storage systems consist of the following categories: (1) solid oxide fuel cells (SOFCs), (2) batteries, (3) electrochemical capacitors and (4) dielectric capacitors. From the Ragone plot, one can see that the SOFCs have the highest energy density, while the electrostatic capacitors possess the highest power density, which is up to 10^7 W/kg. In between, the electrochemical capacitors show a tendency of partially replacing batteries due to their fast-growing energy density; see Figure 1. Specifically, the ultrafast charging/discharging rates, at microsecond level, make dielectric capacitors widely used in devices such as motor starters, high-power lasers, signal processing and sensors [3]. In retrospect, the technological advancement may date back to the ferroelectric (FE) phenomena of Rochelle salt found by Valasek in 1921 [4,5]. During World War II [6], the discovery of $BaTiO_3$ and its usage in high-energy-density capacitors launched a research boom in the field of FE materials. Possibly enlightened by the whimsical concept of antimatter introduced by Schuster in 1898 [7], Néel and Kittel proposed the concepts of antiferromagnet and antiferroelectric (AFE) in 1936 and 1951, respectively, to explain magnetic and dielectric anomalies at Curie temperature (T_C) [8,9].

Although receiving less attention than FEs, AFE materials have been investigated for their intriguing physical properties, including the origin of antiferroelectricity [10–13], electromechanical coupling [14], electrocaloric effect [15–17] and negative capacitance [18]. In fact, AFE-based materials have been proposed to design memory devices [19,20]. In recent years, both AFE-based and relaxor FE (RFE)-based capacitors [21–26] have been widely investigated due to their reducible energy loss [22,27], improvable maximum polarization (P_{max}), breakdown electric field (E_B) [28–30] and energy efficiency (η) [31,32]. Recently, a series of promising data have been reported [32–36]. Using a superparaelectric design, Pan et al. achieved very high recoverable energy density (J_{rec} = 152 J/cm^3) in $BiFeO_3$-$BaTiO_3$-based RFE thin films [21,37,38]. By means of Sr doping, Acharya et al. reported ultrahigh energy efficiency (η = 97%) in AFE $Pb_{1-x}Sr_xHfO_3$ thin films [39], where the J_{rec} and E_B were 77 J/cm^3 and 5.12 MV/cm, respectively. More surprisingly, Hou et al. found the highest energy density reported thus far (J_{rec} = 307 J/cm^3) in $SrTiO_3/La_{1-x}Sr_xMnO_3$ (STO/LSMO, x ≈ 1/3) thin films, which have values of P_{max} ≈ 125 μC/cm^2, efficiency η ≈ 89% and E_B ≈ 6.8 MV/cm [28]. For representative dielectric films and bulks, a comparison of their energy storage performance is shown in Table 1.

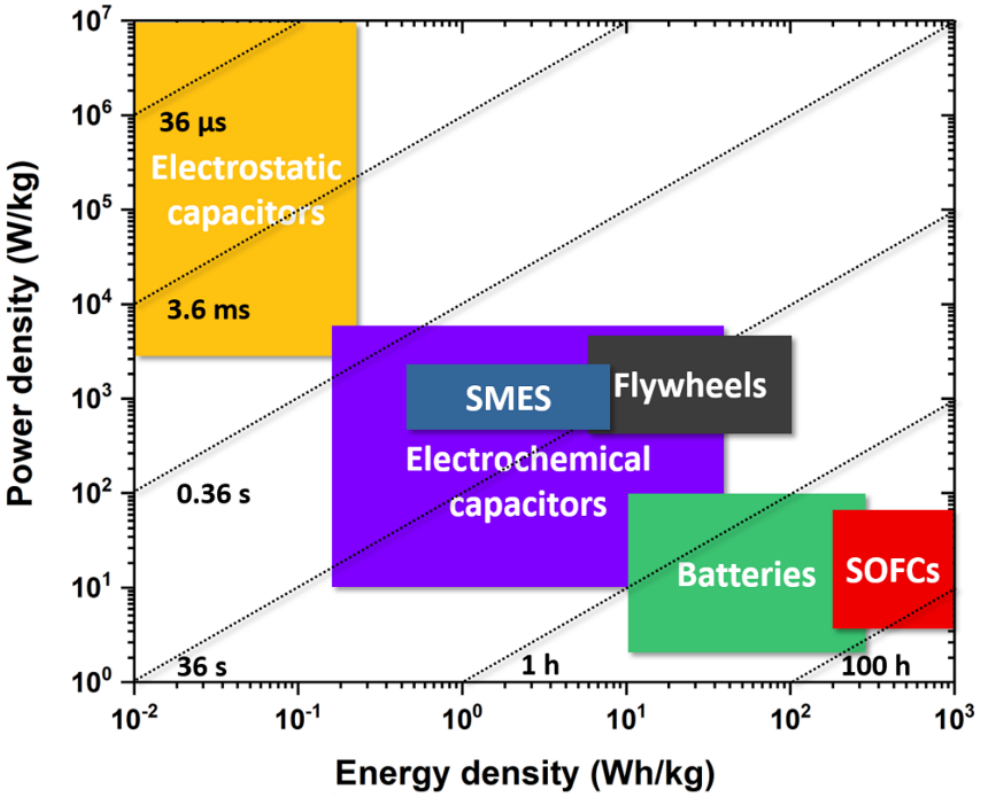

Figure 1. Log-scale Ragone plot showing a performance comparison between different energy storage devices, including superconducting magnetic energy storage (SMES). Conceptually, the energy density (Wh/kg, vertical axis) describes how much energy is available, while the power density (W/kg, horizontal axis) shows how quickly the energy can be delivered. The sloping lines indicate the required time to get the charge in or out of a device [40].

Table 1. Comparison of energy storage performance between representative dielectric films and between representative dielectric bulks.

Dielectric Films	J_{rec} **(J/cm^3)**	η **(%)**	P_{max} **(μC/cm^2)**	E_B **(MV/cm)**	**Ref.**
$SrTiO_3$ (1)	307	89	~125	6.8	[28]
La-Ba-Zr-doped $(Na_{0.5}Bi_{0.5})TiO_3$ (1)	154	97	113.5	3.5	[37]
Sm-doped $BiFeO_3$-$BaTiO_3$ (2)	152	> 90	~60	5.2	[38]
$BaZr_{0.35}Ti_{0.65}O_3$ multilayer (2)	130	73.8	52	8.75	[41]
Mn-doped $Na_{0.5}Bi_{0.5}TiO_3$-$BaTiO_3$-$BiFeO_3$ (3)	102	60	124	2.86	[42]
La-doped Pb(Zr,Ti)O_3 (4)	85	65	115	4.5	[43]
$Pb_{0.5}Sr_{0.5}HfO_3$ (5)	77	97	~53	5.12	[39]
Dielectric bulks	J_{rec} **(J/cm^3)**	η **(%)**	P_{max} **(μC/cm^2)**	E_B **(MV/cm)**	**Ref.**
$Na_{0.5}Bi_{0.5}TiO_3$-$Sr_{0.7}Bi_{0.2}TiO_3$ (3)	21.5	~80	67	103	[36]
0.90$NaNbO_3$-0.10$BiFeO_3$ (6)	18.5	78.7	64	~1.0	[44]
La-doped $Pb(Zr_{0.55}Sn_{0.45})_{0.995}O_3$ (7)	10.4	87	41.3	0.4	[32]
$(Pb_{0.91}Ba_{0.045}La_{0.03})(Zr_{0.6}Sn_{0.4})O_3$ (7)	8.16	92.1	40	0.34	[31]
$BiFeO_3$-$BaTiO_3$-$NaNbO_3$ (6)	8.12	90	~52	0.36	[45]
$AgNbO_3$-$AgTaO_3$ (6)	7.5	86	32	0.53	[46]

Note: The bottom electrode types are (1) $La_{0.67}Sr_{0.33}MnO_3$, (2) Nb-$SrTiO_3$, (3) Pt, (4) $LaNiO_3$, (5) $SrRuO_3$, (6) silver paste, (7) Au.

Given a "mismatched" structure–property relationship, one may naturally ask: how does a nonpolar $SrTiO_3$ deliver such a high P_{max} value and energy storage density? Although static structural and compositional characterizations are very helpful, in situ phase transition and storage pathway studies are more promising in unveiling the hidden mysteries. Compared with macroscopic property investigation, in situ dynamic structure study lags far behind in the field of dielectric capacitors. An important reason lies in the fact that there exists a large mismatch between the structural response time for energy storage [47] and the data collection time [48–50]. For the former, this is usually completed at the millisecond scale or within an even shorter time. Meanwhile, for the latter, e.g., X-ray diffraction (XRD) and selected area electron diffraction (SAED), they usually take several seconds or even minutes in collecting a dataset. In comparison with RFEs [21,23,51], AFEs are more widely investigated in structural phase transitions under in-situ conditions. The reason resides in the fact that the AFE-to-FE transitions inherently couple with the energy storage process [32,52–54].

Building on the established phase transition framework, this review seeks to broaden the research scope from AFEs to nonpolar materials, which are simultaneously ferroelastic or antiferroelastic, in the quest for promising energy storage materials. Under in situ conditions, this entails the extension of well-known AFE-to-FE transition to broader antiferrodistortive-to-ferrodistortive (AFD-to-FD) transition. By summarizing external field-driven phase transitions, research progress regarding in situ and atomic-scale structural characterization, achieved by using direct light-element imaging, is highlighted to understand the energy storage mechanism. Associated with ionic migration across the dielectric/electrode interface, we further discuss the electric field-driven metal-to-insulator (M-I) transition in electrodes and its potential impact on tuning the macroscopic energy storage density of dielectric capacitors.

2. Fundamentals of Capacitor Energy Storage

A dielectric capacitor is constructed in a parallel-plate form, i.e., a dielectric layer sandwiched by two conductive electrodes. The physical quantity that manifests the energy storage is capacitance (C), which can be described by the following equation:

$$C = \varepsilon_0 \varepsilon_r A/d \quad (1)$$

where ε_0 is the dielectric permittivity in vacuum (~8.85 × 10^{-12} F/m), ε_r (>> 1) is the relative dielectric constant of the dielectric layer, A is the overlapping area of the electrodes, and d is thickness of the dielectric layer. In principle, the capacitance only depends on the geometry of the capacitor and permittivity of the dielectric layer. However, this is not always the case, especially when electric field-driven electrochemical activities take place near the dielectric/electrode interface, as discussed below.

When an external voltage is applied, charges with opposite signs and equal magnitude accumulate at the electrodes. This is the so-called charging process. The charges form an internal electric field, whose direction is opposite to that of the external electric field. The charging process finishes when the internal electric field induced by the accumulated charges ($Q = CV$) is equal to the external field ($E = V/d$), where V is the applied voltage. During the charging process, the charges are moved by the external electric field, and electrostatic energy is stored in the dielectric layer. The stored energy can be calculated from the following expression:

$$W = \int_0^{Q_{max}} V dq \quad (2)$$

where $Q_{\max}$ is the maximum charge when the charging process finishes, and dq is an increment of charge. One of the key figures of merit of the dielectric capacitor is its energy density (J), which measures its "capability" for storage performance and can be written in the following form:

$$J = \frac{W}{Ad} = \int_0^{P_{max}} E dP \quad (3)$$

The energy density can therefore easily be obtained by integrating the area between the polarization and electric field axes in the P-E loop. Another key figure of merit for the capacitor is energy efficiency (η). It is equals to the ratio between the recoverable energy density (J_{rec}) and total energy density (J_{tot}), which can be expressed by

$$\eta = (J_{rec}/J_{tot}) \times 100\% \quad (4)$$

where the J_{tot} is a sum of the P-E loop (J_{loss}) and its left-side area (J_{rec}) at $E \geq 0$ in the P-E relation chart (see Figure 2b). It appears that a linear dielectric, with $J_{rec} \approx \frac{1}{2}\varepsilon_0 \varepsilon_r E^2$ and very small J_{loss}, may offer higher storage density. In practice, phase transition materials offer much higher energy storage densities due to their much larger E_B and maximum polarization (P_{max}), which can be one order of magnitude higher than that of linear dielectrics [39,55]. As for more circuit-related details of energy storage measurement, this has been discussed elsewhere [24,40].

From a microstructure point of view, complex structural changes take place during the charging process. Inside the nonpolar dielectric layer, this involves inversion symmetry breaking and the emergence of electric dipoles from the originally centrosymmetric lattices. Irrelevant to either displacive or order–disorder phase transition [56,57], the electric dipoles are defined by the separation of positive and negative charge centers within each unit cell. At mesoscopic scale, this is affected by phase constitution, domain reorientation and growth, defect type and density. Near the dielectric/electrode interface, polarization screening, chemical diffusion, ionic migration and potential M–I transition significantly impact the energy storage and release. Therefore, unveiling the dynamic structural responses under in situ conditions may greatly deepen our mechanistic understanding, which is essential for the development of new materials and devices.

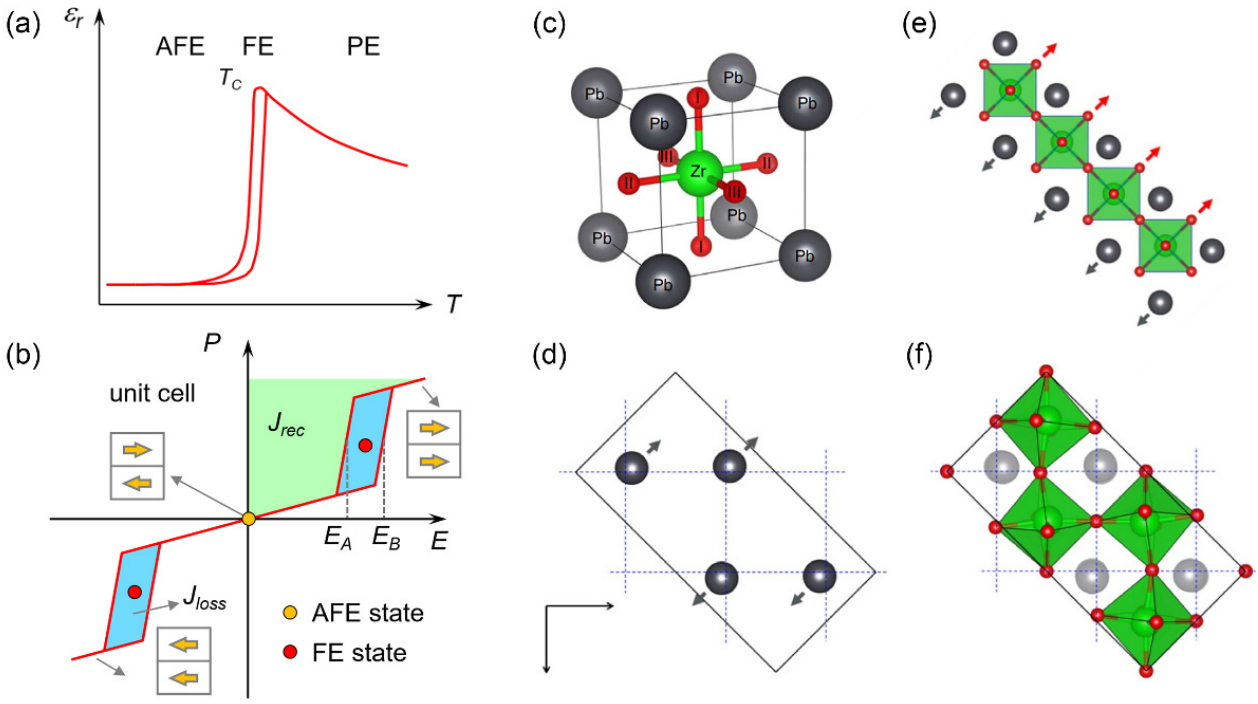

Figure 2. Dielectric constant (ε_r), P-E loop and structural phases of $PbZrO_3$. (**a**,**b**) Temperature-dependent ε_r and hysteresis loop of AFEs. The green and blue shaded areas in (**b**) denote recoverable (J_{rec}) and loss (J_{loss}) energy during the AFE-to-FE transition. (**c**) Unit cell of the cubic $PbZrO_3$ phase (space group $Pm\bar{3}m$). (**d**–**f**) Antiparallel Pb displacements (Σ mode), polar displacement (Γ mode) and oxygen octahedral rotations (R mode) in AFE $PbZrO_3$ (space group *Pbam*), respectively. The dotted lines show the cubic crystallographic axes in the ab plane [10].

3. Structural Features and Phase Transitions in Antiferroelectrics

FEs undergo a nonpolar-to-polar transition at T_C and the breaking of spatial inversion symmetry leads to the emergence of spontaneous polarization (P_S) in the low-temperature phase. Under the application of an electric field (E), the direction of polarization (P) in domains can be reversed and its nonlinear response to E gives rise to a P-E hysteresis loop. Depending on the category of the FEs, the hysteresis loop may vary between a square shape (e.g., in $BaTiO_3$) [58] and a slim shape (e.g., in relaxor $Na_{0.5}Bi_{0.5}TiO_3$) [37]. Thus, the energy consumption is usually larger for the former than the latter due to its larger P_r (a value at $E = 0$) and loop areas. In contrast, AFEs undergo a phase transition between two nonpolar phases at T_C, around which an FE phase may transiently exist in a narrow temperature window [59–61]; see Figure 2a. Despite zero spontaneous polarization at $T < T_C$, a strong E can drive an AFE-to-FE phase transition [52,62], which gives rise to a double hysteresis loop; see Figure 2b. Due to the concave curvature of the P-E relationship, with a reflection point at coercive field E_A or E_B, the AFEs usually possess intrinsically high energy storage densities [63].

In a crystal structure, an important feature of AFE is that its unit cell volume is doubled with respect to its paraelectric (PE) phase (Figure 2c). Benefiting from the antiparallel arrangement of electric dipoles within sublattices, null polarization is obtained on the unit cell scale. Typical AFE systems include $PbZrO_3$, $AgNbO_3$, $NaNbO_3$, HfO_2 [64–72] and recently reported 2D van der Waals AFE β'-In_2Se_3 [73,74]. From the perspective of lattice dynamics, the emergence of antiferroelectricity is a consequence of competing lattice instabilities [10,11], which are manifested by delicate structural orders [66,75]. Taking $PbZrO_3$ as an example, its AFE phase is dominated by antiparallel Pb displacements along the $[100]_O//[110]_c$ direction (O: orthorhombic; c: pseudocubic) and antiferrodistortive (AFD) oxygen octahedra ($a^-a^-c^0$ in Glazer's notation) [66]. The corresponding Σ and R modes in the Brillouin zone (Figure 2d,f) are represented by wave vectors of

$\mathbf{k}_\Sigma$ = (2π/a)(1/4, 1/4, 0) (*a* is the cubic lattice constant) and $\mathbf{k}_R$ = (2π/a)(1/2, 1/2, 1/2), respectively [10,11].

A polar instability, i.e., the Γ mode, manifested by opposite shifts of Pb cations and oxygen anions, is responsible for ferroelectricity (Figure 2e). In the ground state, the polar instability is suppressed due to its higher energy level. Nevertheless, it has been shown that the energy levels of different lattice instabilities can be subverted in the following situations. (1) Application of large *E* can destabilize the Σ and R modes and drive an AFE-to-FE transformation [76–78]. (2) Interruption of the cationic displacement order and AFD order at translational boundaries allows the emergence of local ferroelectricity with a bi-stable feature [79–81]. (3) An intrinsic surface effect may trigger an AFE-to-FE transition as the sample thickness is below a critical thickness, ~6.5 nm for $PbZrO_3$ [82,83]. (4) Chemical doping can also alter the cationic displacement order and AFD order, e.g., stochastic stacking of Pb-displacement-based stripes in La-doped $PbZrO_3$. Due to the uncompensated antiparallel arrangement of Pb cations, weak ferrielectricity emerges in doped systems [84–86].

4. Antiferrodistortive and Ferrodistortive Phase Transitions

In fact, both FE-to-PE and AFE-to-PE transitions can be understood from the viewpoint of ferroelastic phase transition, which is related to a change in lattice symmetry around T_C [87,88]. In many cases, ferroelasticity or antiferroelasticity is a secondary or improper effect, since the driving force is related to cation or molecular ordering and the softening of optical phonon branches [89,90]. Thus, a large proportion of ferroelastic transitions depend on mode condensation at a position in the Brillouin zone. When modes condense at zone boundaries, the transition is termed AFD [91]. For a perovskite, the AFD order is manifested by in-phase and out-of-phase rotation of the oxygen octahedra [92,93]. Thus, the AFEs constitute a subgroup of AFD transitions (Figure 3a,b). In contrast, when modes condense at the zone center, the transition is termed FD. Correspondingly, the FEs constitute a subgroup of FD transitions (Figure 3c,d). It should be noted that the AFD phases are characterized by the rigid octahedral linking through out-of-phase tilting, in-phase tilting or their combination. In FD phases, associated with symmetry lowering, polar octahedral distortion can modify or destroy the rigid linking and response to the applied electric field together with A-site cations. In addition, there are also antipolar (AP) and pyroelectric (PyE) phases, which belong to the subgroups of AFD and FD transitions, respectively. In contrast to AFE and FE phases, their dipoles cannot be reversed, even by a strong electric field [91].

It should be noted that the zone-center mode condensation is not necessarily bound to the zone-boundary condensation in proper FEs. This means that the polar order can either be irrelevant to the AFD order (e.g., in $BaTiO_3$ and $PbTiO_3$) or couple cooperatively with the AFD order (e.g., in $BiFeO_3$, $ZnSnO_3$ and $ScFeO_3$) [94–96]. Besides the routine manifestations, as a counterpart of AFD, the FD phase transition may place extra emphasis on a means of inducing ferroelectricity through the long-range polar distortion of oxygen octahedra. This broadens the perspectives of understanding the origins of ferroelectricity and implies that more nonpolar dielectrics with typical AFD order [92,93] can be transformed to novel FD phases under excitation of an external field [97]. Being compatible with chemical, defect and strain engineering [30,98], therefore, the range of candidate energy storage systems can be greatly expanded by the AFD-to-FD transition.

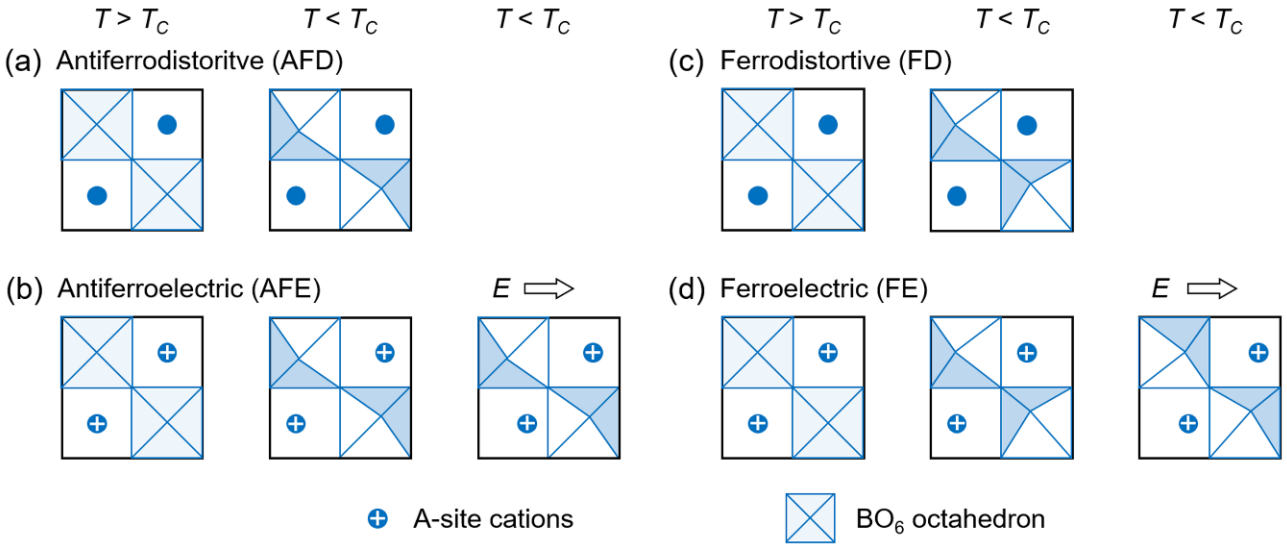

Figure 3. Structural phase transitions of a centrosymmetric perovskite oxide (ABO_3). (**a,c**) Antiferrodistortive (AFD) and ferrodistortive (FD) transitions caused by temperature or stress, respectively. Out-of-phase or in-phase octahedral rotation is linked in (**a**) but can be unlinked in (**c**) due to polar distortion. (**b,d**) Antiferroelectric (AFE) and ferroelectric (FE) transitions caused by temperature and electric field E, respectively. Associated with symmetry lowering, polar octahedra in an FD phase may respond to applied electric field together with A-site cations.

With reference to the above classifications, the STO/LSMO system, with ultrahigh energy density (307 J/cm^3) at a thickness range of 410~710 nm for STO, provides a good example to analyze the AFD-to-FD transition [28,99]. It has been widely accepted that the cubic $SrTiO_3$ (space group $Pm\bar{3}m$) transforms to a tetragonal structure ($I4/mcm$) via a second-order AFD phase transition at T_C = 105 K. Below T_C, the tetragonal phase is characterized by the antiphase rotation of the octahedra along its c axis ($a^0a^0c^-$ in Glazer's notation) [100]. The temperature–strain phase diagram [101–104] shows that the FE phase can be stabilized through strain engineering (Figure 4a). Nonetheless, the following results indicate that the mechanism leading to polarity in $SrTiO_3$ is not that simple. Compared with strained $SrTiO_3$, Jang et al. demonstrate that strain-free $SrTiO_3$ is an RFE, with a temperature for the maximum ε_r at $T_m \approx 45$ K [29]. The role of strain is to stabilize the long-range correlation of preexisting nanopolar regions; see Figure 4b,c. Another argument points out that the abnormal ferroelectricity at $T < T_m$ arises from FE antiphase boundaries [105–107]. Similar to AFE $PbZrO_3$, once the nonpolar lattice instabilities become destabilized, the "hidden" polar lattice instability prevails and gives rise to the ferroelectricity.

Excited by either an optical pump or a THz electric field (with a threshold field amplitude of ~300 kV/cm), two research groups independently reported that metastable ferroelectricity with $T_C \approx 290$ K can be achieved in $SrTiO_3$ [102,108]. By introducing Ti/O-deficient nanoregions [30], Li et al. showed that defect engineering can also drive the occurrence of AFD-to-FD transition. Using this strategy, they realized a very large lattice tetragonality ratio (c/a = 1.038), strong room-temperature ferroelectricity (P_S = 41.6 μC/cm^2) and very high T_C (~1098 K) in $SrTiO_3$ films; see Figure 4d. Using first-principles calculations, Klyukin and Alexandrov reported that antisite defects, either Ti on a Sr site (Ti_{Sr}) or vice versa (Sr_{Ti}), can result in large electric polarization in $SrTiO_3$ [109–111]. These outcomes suggest that structural defects should play an important role in achieving ultrahigh polarization in the STO/LSMO system (see inset of Figure 4d). More importantly, this sets a precedent for retrofitting other nonpolar perovskites into energy storage media via chemical and defect engineering, e.g., $CaTiO_3$ and $DyScO_3$ [55,98,112].

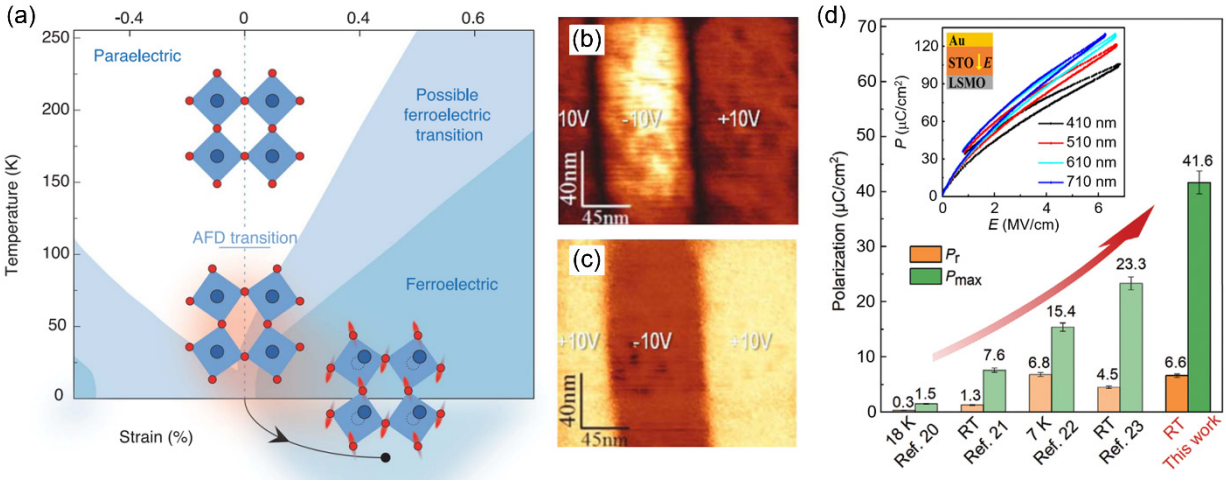

Figure 4. Structural phase transition and FE properties of $SrTiO_3$. (**a**) Temperature–strain phase diagram showing an AFD transition and a further FE transition [102]. (**b**,**c**) Piezoresponse force microscopy (PFM) amplitude and phase images of strain-free $SrTiO_3$ films recorded at 50 K at biasing voltages of ±10 V [29]. (**d**) Comparisons of P_r and maximum polarization (P_{max}) between Ti/O-deficient $SrTiO_3$ (P_r = 6.6 μC/cm^2, P_{max} = 41.6 μC/cm^2) and the literature cited therein [30]. The inset shows the *P*-*E* loops measured from the Au/$SrTiO_3$/LSMO (x ≈ 1/3) capacitors [28].

5. Anisotropic Energy Storage

The double *P*-*E* hysteresis loop shown in Figure 2b indicates that synergistically changing the following parameters may optimize the energy storage performance: (1) simultaneously increasing the critical electric fields E_A and E_B and minimizing the loop area [31]; (2) increasing the P_{max} [28] and minimizing the P_r [32]. In practice, due to the dielectric anisotropy of the crystals [113], the energy storage density of identical materials also exhibits a direction-dependent nature [71,97,114,115]. Taking $PbZrO_3$ as an example, multiscale first-principles computations show that as the *E* is applied along different crystallographic directions, its phase transition pathways are distinct (Figure 5a). On this basis, Lisenkov et al. found three high-strain polar phases: a monoclinic (*Cc*) phase, an orthorhombic (*Ima2*) phase and a tetragonal (*I4cm*) phase [114].

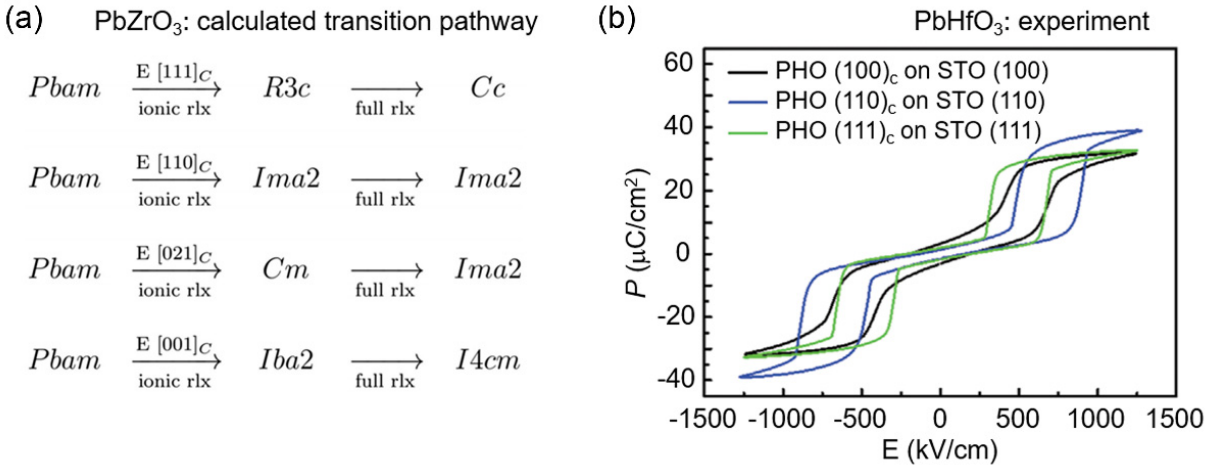

Figure 5. Anisotropic energy storage pathways. (**a**) Predicted phase transition pathways for $PbZrO_3$ associated with ionic and full structural relaxation after applying electric fields along different crystallographic directions. The multiscale structure prediction combines classical and first-principles density functional theory [114]. (**b**) Structural anisotropy-dependent energy storage performance of AFE $PbHfO_3$ thin films grown on different crystal-plane-terminated $SrTiO_3$ substrates [71].

In experiments, the key electrical parameters relating to energy storage also show strong crystal orientation dependence. AFE (200 nm) $PbHfO_3$ films grown on $(100)_C$-plane, $(110)_C$-plane and $(111)_C$-plane terminated $SrTiO_3$ substrates, which are buffered by $SrRuO_3$ electrodes, are good examples that confirm this [71,72]. Together with large changes in critical field and P_r, the P_{max} takes values of 30.54, 38.91 and 32.64 $\mu C/cm^2$ in the three films, respectively (Figure 5b). Corresponding to a larger coercive field and P_{max}, the $(110)_C$ oriented film delivers higher energy storage density (J_{rec} = 21.4 J/cm^3) than the other two ($J_{rec} \approx 16$ J/cm^3) [71]. From a microstructural perspective, one may expect that the type and density of structural defects [116–119] may influence the energy storage performance. Through introducing local compressive pressure, Zhang et al. reported that enhanced critical fields may increase the J_{rec} [53,67,120], e.g., from 9 to 16.2 J/cm^3 in Li^+-La^{3+} co-doped $PbZrO_3$ films. By constructing a ferrielectric (FiE) M2-M3 phase boundary, Luo et al. achieved an energy density of 6.3 J/cm^3 with η = 90% in (1-x)$AgNbO_3$-x$AgTaO_3$ solid solution [46].

6. In Situ Structural Shase Sransition Sathway

In conjunction with macroscopic property measurement, in situ dynamic structural studies can help to construct structure–property relationships directly. Under the application of an electric field, answers to the following questions are expected to play critical roles in further improving the energy storage performance. Q1) How does electrical polarization emerge and evolve from a nonpolar lattice matrix? Q2) What are the key structural factors that control and limit critical fields (E_A and E_B), P_{max} and P_r? Although the phase transition processes are complex, as reported in $PbZrO_3$-based and $NaNbO_3$-based systems [121–124], manipulative free dimensions about spatial, temporal and electric field offer a plethora of opportunities to unveil the unknowns. For example, in $Pb(Zr_{0.57}Sn_{0.43})O_3$-based ceramics, Fan et al. observed local depolarization field-assisted AFE-to-FE transition during monotonic E loading using in situ (scanning) transmission electron microscopy (S/TEM). In addition to this, they also found suppression of FE domain mobility after 10^3-time bipolar cycling, which indicates the electric fatigue of the FE phase [125].

By largely improving the temporal resolution under in situ biasing conditions, from ~30 s to 415 ms per data pattern, Zhang et al. investigated the dynamic structure evolution of polycrystalline $NaNbO_3$ using high-energy XRD (Figure 6a). Associated with the disappearance and appearance of specific superlattice reflections, e.g., $\frac{1}{2}(312)_c$ reflection, they found that an AFE-to-FE transition took place around E = 8 kV/mm [126]. At E > 12 kV/mm, abruptly enhanced polarization and longitudinal strain S_{33} indicated the transformation of the nonpolar P phase (orthorhombic AFE, *Pbcm*) to the polar Q phase (orthorhombic FE, $P2_1ma$) (Figure 6b–d). According to the mismatch of the P-phase fraction with changes in lattice parameter, volume, polarization and S_{33}, they proposed a decoupled polarization switching process in the range of 8 < E < 12 kV/mm. Given that the P phase ($a^-a^-b^+/a^-a^-b^-/a^-a^-b^+$) differs from the Q phase ($a^-a^-b^+$) in octahedral tilting, the field-dependent structural data cannot exclude another possibility, i.e., the existence of an intermediate FiE phase. It adopts a Q-phase structural framework [98], but the oxygen octahedra are in a transitional state. Observation of weak ferrielectricity in $PbZrO_3$-based ceramics supports this possible interpretation [85,86,127].

Compared with diffraction-based techniques, E-dependent structural transition, measured at atomic scale using S/TEM, provides more intuitive information about energy storage. However, even using a state-of-the-art imaging detector such as the K3 camera, which is capable of collecting 1500 data frames per second (0.67 ms per frame), the mismatch in time remains due to the requirement of sufficient signal intensity and image contrast for data analysis. Thus far, several advanced imaging techniques have been used to image light elements, e.g., negative spherical aberration imaging (NCSI) [128–130], annular bright field (ABF) imaging [131], integrated differential phase contrast (iDPC) imaging [132,133] and electron ptychography [134]. Despite this, imaging light elements such as oxygen under in situ biasing conditions remains a challenge due to their very low

scattering power. As a compromise, slowing down the phase transition speed becomes a good solution to unravel the evolution of characteristic structural orders as a function of field strength and time [52].

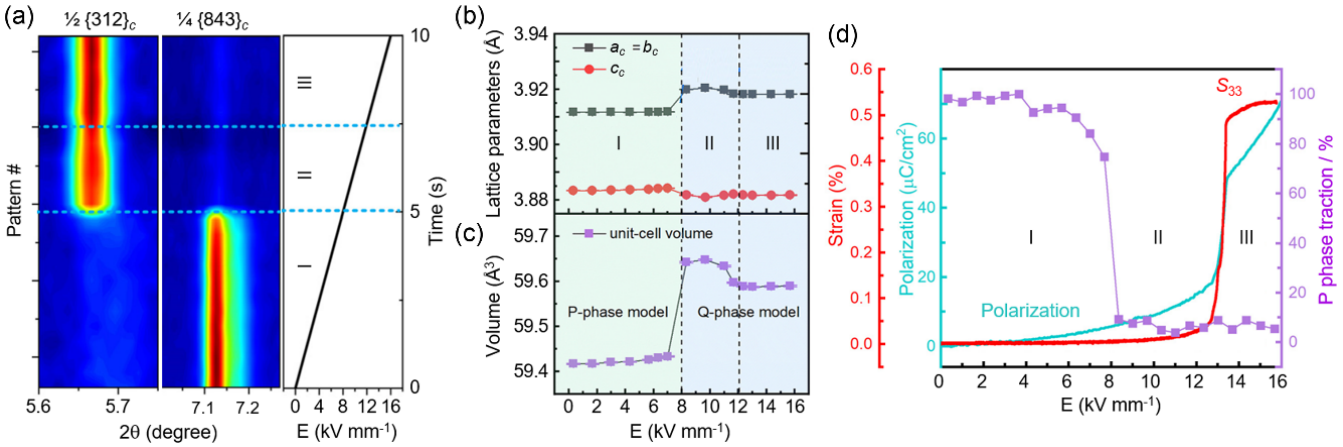

Figure 6. Time-dependent phase transition in $NaNbO_3$ under excitation of electric field. (**a**) Evolution of XRD superlattice reflections with increasing electric field for the AFE P (stage I) and FE Q (stage III) phases. (**b,c**) Pseudocubic lattice parameters and unit cell volume plotted as a function of electric field amplitude. (**d**) Evolution of the P-phase fraction, macroscopic polarization and longitudinal strain S_{33} as a function of electric field [126]. Instead of the decoupled polarization switching process, stage II may also be interpreted as the emergence of an intermediate FiE phase.

Recently, Wei et al. found that an illumination electron beam in a TEM can act as an external electric field to trigger phase transitions in dielectric insulators. The principle lies in the fact that the electrons captured by the insulating sample surface are "equivalent" to the electrostatic charging effect [135,136]. By slowing down the phase transition speed to the level of seconds, the investigation of atomic-scale structural changes becomes possible [127,137,138]. For a $[001]_O$-oriented $PbZrO_3$ lamella sample, time- and atomic-resolution NCSI-TEM study [127] reveals that the AFE-to-FE transition involves the splitting of pseudocubic a_p and b_p axes. As a function of irradiation time, the unit cell volume undergoes a reduction-to-expansion transition as the AFE phase evolves into FE monoclinic (FE_M) and rhombohedral (FE_R) phases (Figure 7a–e). During the in situ energy storage process, an intermediate transient FD phase was observed between the AFE and FE phases. With the preservation of antiparallel Pb displacements, polar octahedral distortion takes place and breaks the spatial inversion symmetry along the x direction. Associated with the extraction of atomic positions through quantitative TEM study, the authors found that the transient FD phase exhibits a cycloidal order of polarization, with $P_S \approx 2.8$ μC/cm^2 (Figure 7c,f). The finding of this FiE phase suggests the origin of the linear polarization response at $E < E_{A(B)}$ in the *P-E* loop of $PbZrO_3$. Synchrotron X-ray and neutron diffraction structural studies reported similar FiE behavior, characteristic of a wavy polarization order, in ternary $PbZrO_3$-$PbSnO_3$-$PbTiO_3$ solid solutions [85,86,139].

Regarding the phase transition pathway, we should note the possible difference between calculated models and experimental observations (Figures 5 and 7). For the latter, structural defects such as atomic vacancies and stoichiometry issues prevail in real samples [140,141], and they may potentially influence the transition pathway. By using time- and atomic-resolution NCSI-TEM, Wei et al. found that a defect core, induced by oxygen and Pb vacancies [118], can act as a seed to trigger unit-cell-wise AFD-to-FD transition in $[001]_O$-oriented $PbZrO_3$ (Figure 8a–e). This is in sharp contrast to the case with the absence of such a defect core, where a relatively uniform AFD-to-FD transition takes place in the region irradiated by the electron beam [127]. As a result of the seed effect, charged FD domains with head-to-head and tail-to-tail configurations are observed during the energy storage process.

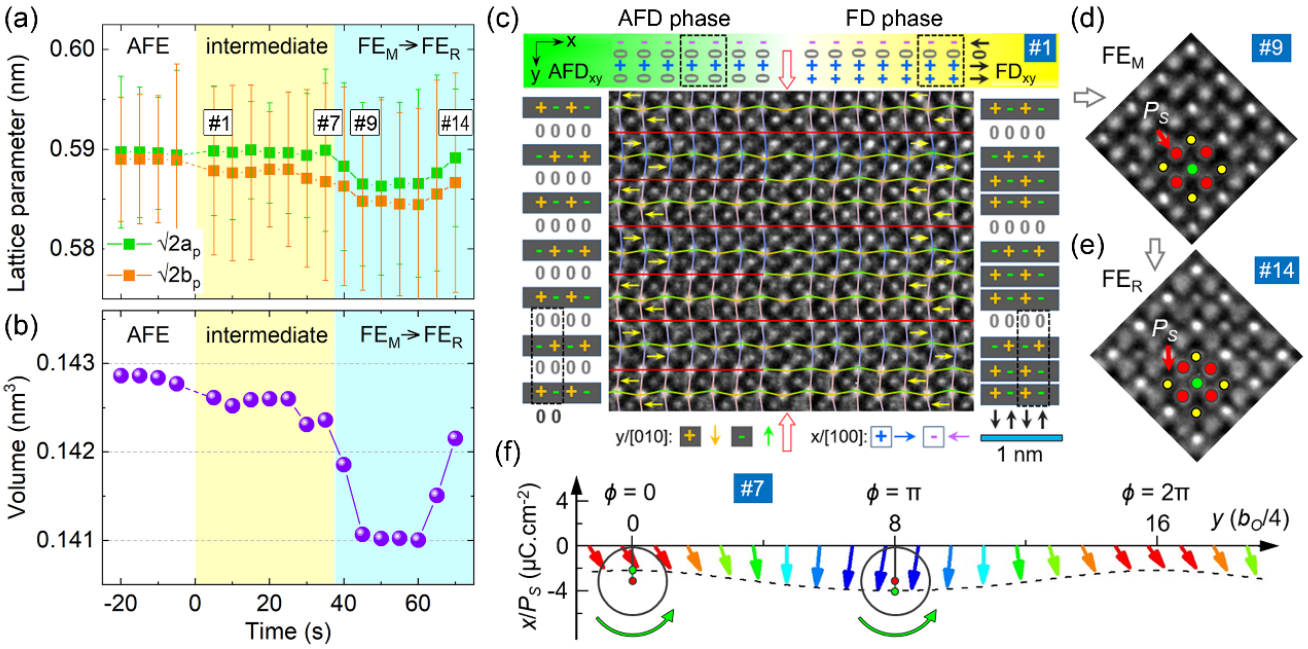

Figure 7. Structural phase transitions of $PbZrO_3$ induced by electron-beam irradiation in a TEM. (**a**,**b**) Changes in lattice parameter ($\sqrt{2}a_p$, $\sqrt{2}b_p$) and volume ($V = \sqrt{2}a_p \times \sqrt{2}b_p \times c_p$) plotted as a function of irradiation time, respectively. (**c**–**e**) Atomic-resolution NCSI-TEM images of an AFD-FD phase boundary and associated structural phase transitions recorded along $[001]_O$ direction, respectively. The oxygen displacements in (**c**) are indexed by (+, 0, –) symbols and colorful solid lines. The yellow arrows denote antiparallel Pb displacements. The atom types are Pb—yellow, Zr—green, O—red circles, respectively. (**f**) 2D cycloidal order of polarization for the transient FE-FD phase obtained using quantitative TEM study [127].

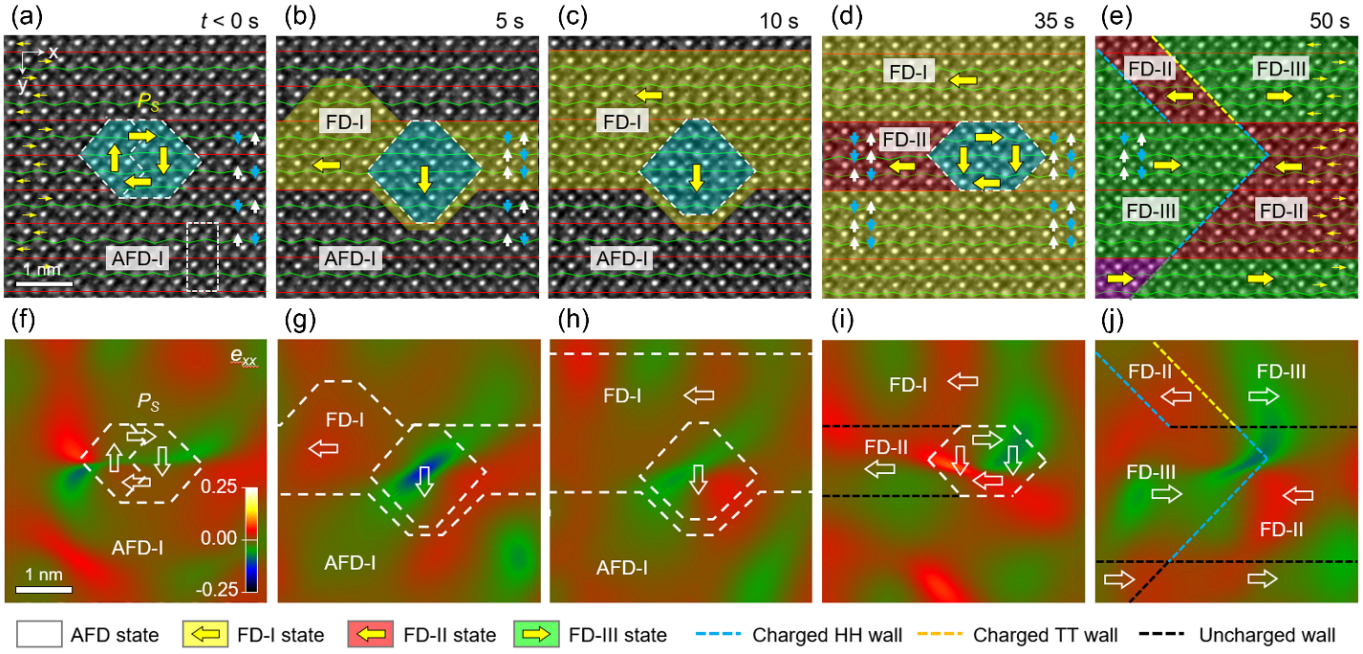

Figure 8. Defect-core-induced unit-cell-wise energy storage pathway in $[001]_O$-oriented $PbZrO_3$. (**a**–**e**) Phase and domain structure evolution as a function of electron-beam irradiation time (dose rate = 3.8×10^6 e/nm^2·s). The cyan shadow and thick yellow arrows denote the defect core and polarization, respectively. (**f**–**j**) Corresponding lattice strain e_{xx} (horizontal $[100]_O$ direction) maps obtained using geometric phase analysis (GPA) [118].

Compared with neutral domain walls, we know that the formation energy of charged domain walls is much higher [117,142] and 2D electron gas may form at the walls to compensate for bound charges and lower the electrostatic energy [113,143]. The anisotropic structural transformation suggests that the defect cores probably lower the coercive field (E_B). With the preservation of antiparallel Pb displacements, this further proves that the energy storage and transfer begin with distorting the oxygen octahedral network. Another point worth noting is the evolution of the polar configuration inside the defect core. At the initial AFE state, electric dipoles form a self-compensated vortex structure. Accompanied by energy injection, the local polarity is stabilized until immersion in the FD states. Strain analysis reveals that nanoscale local compressive strain leads to the seed effect of the defect core (Figure 8f–j). This points out that the rational selection of the doping element and concentration is crucial for optimizing the storage performance of dielectrics [144–146].

7. Ionic Migration across Dielectric/Metal Interfaces

In oxide-based dielectric capacitors, metallic $(La_{1-x}Sr_x)MnO_3$ [147], $(La_{1-x}Sr_x)CoO_3$ [148] and $SrRuO_3$ [149] are standard choices for bottom electrodes. Previous transport property studies have reported that $(La_{1-x}Sr_x)MnO_3$ undergoes thickness-driven and electric-field-driven M–I transition [137,150,151]. When such a transition occurs in dielectric capacitors, "dead" layers appear at the dielectric/electrode interfaces and this may impact the energy storage performance. Driven by the depolarization effect, the "dead" layers usually lead to reduced capacitance near the interface [152–154]. The contrary phenomenon observed in the STO/LSMO system ($P_S \approx 125$ μC/cm^2) suggests that the interface should contribute positively to the "defect-induced" ferroelectricity in $SrTiO_3$ (Figure 4d). Hou et al. ascribe the enhanced E_B to the modulation of the local electric field and redistribution of oxygen vacancies at the oxide interface [28]. However, the finite interface thickness (~5 nm), compared to that of ~560 nm for $SrTiO_3$, casts doubt on the role of the interfacial contribution alone.

Rhombohedral LSMO (x ≈ 1/3, space group $R\bar{3}c$) has a ferromagnetic metallic state at room temperature. Below $T_C \approx 367$ K, its structure is characterized by AFD octahedral rotations ($a^-a^-a^-$ in Glazer's notation) [147,155]. By using in situ biasing STEM, Yao et al. revealed an *E*-induced M–I transition by measuring the *E*-dependent resistivity change. The insulating state was attributed to the formation of a brownmillerite (BM) phase (*C*2/*c*), which has a bandgap of $E_g \approx 0.63$ eV [151,156,157]. In $Hf_{0.5}Zr_{0.5}O_2$ (HZO, 5 nm)/LSMO films (Figure 9a), Nukala et al. directly observed oxygen vacancy-induced structural transition in bottom LSMO by using in situ biasing iDPC STEM [158]. In addition to an intermediate BM precursor phase, they found the intertwining of polarization switching with the migration of oxygen vacancies (Figure 9b–d). Specifically, the role of the dielectric oxide layer, either as a fast conduit or as a source/sink of oxygen migration depending on the oxygen reactivity of the top electrode [158,159], highlights the necessity of considering electrochemical activities for capacitors under working conditions. This may involve the migration of atomic vacancies and cations through antisite defects, and electronic structure changes in all atomic species. The ultrahigh energy density achieved in Na-based perovskite oxides, e.g., ionic conductor $(Na_{0.5}Bi_{0.5})TiO_3$ [160], also suggests the important role of ionic migration in enhancing the energy storage performance; see Table 1. In addition, possible FE metal states [161–163] should be considered at the dielectric/metal interfaces. These mechanisms may apply to the nonpolar Au/STO/LSMO and other systems [164,165].

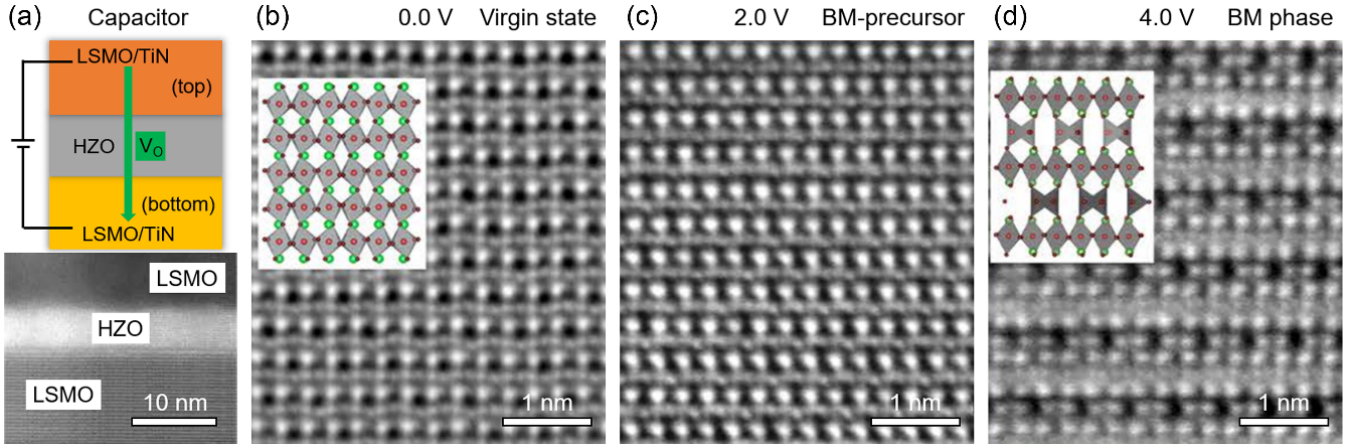

Figure 9. Deoxygenation of the bottom $(La_{1-x}Sr_x)MnO_3$ (LSMO, $x \approx 1/3$) electrode with increasing positive bias in an LSMO/HZO/LSMO capacitor. (**a**) Polarity-dependent oxygen voltammetry process (V_O: oxygen vacancy) and morphology of the dielectric capacitor. (**b–d**) The iDPC-STEM images of a representative region of the bottom LSMO layer, showing (**b**) the virgin 0.0 V state, (**c**) the BM precursor phase (with mixed MnO_5 and MnO_6 polyhedra) at 2.0 V and (**d**) the BM phase at 4.0 V viewed along the $[110]_c$ zone axis. The atom types in the insets are La/Sr—green, Mn—red and O—brown [158].

8. Summary and Outlook

By generalizing the AFE-to-FE transition to a broader AFD-to-FD transition, we summarize in situ phase transition pathway studies in energy storage nonpolar materials. Aiming at identifying the underlying mechanism and improving the energy storage performance of dielectric capacitors, we highlight several key points below to inspire future research.

(I) Besides mesoscale domain structure and phase boundary evolution, light element sensitive imaging techniques should play a key role in unraveling the in situ dynamic phase transition during energy storage. The reason lies in the fact that the delicate energy transfer usually starts from light-element-based structural units, e.g., distortion of the oxygen octahedra and migration of oxygen vacancies. Specifically, transient FE or FiE phases may possibly emerge under non-equilibrium conditions. Apart from deepening our understanding of the energy storage process, such studies promise to expand the recognition scope of FE physics.

(II) Case studies of $PbZrO_3$, $SrTiO_3$ and $(La_{1-x}Sr_x)MnO_3$ highlight the significance of carrying out defect and interface structure investigation during the energy storage processes. This may include dopant-induced strain change, antisite mechanism and phase boundary evolution under in situ biasing conditions. Establishing the direct microstructure–property relationship may help to optimize the figures of merit of the *P-E* loops, e.g., increasing the P_{max} and critical fields while reducing P_r and the loop area.

Finally, two recent works reported that mesoscale-domain engineering may greatly improve the energy storage density, e.g., from 12.2 to 18.5 J/cm^3 in $NaNbO_3$-based relaxor AFE ceramics [44,166]. Pertinent to the beneficial hierarchical domain structures, structure–property relationship study of FE $Pb(Zr,Ti)O_3$ shows that this may arise from phase transition frustration near a tricritical point [167]. Together with the use of advanced computation and simulation methods, such as machine learning, we believe that carrying out cross-scale microstructure study may boost the development of energy storage materials and their device application.

Author Contributions: X.-K.W. conceived the review idea and wrote the manuscript. R.E.D.-B. and J.M. provided full support and revised the manuscript. All authors have read and agreed to the published version of the manuscript.

Funding: This research received no external funding.

Institutional Review Board Statement: Not applicable.

Informed Consent Statement: Not applicable.

Data Availability Statement: Not applicable.

Acknowledgments: X.-K. Wei acknowledges the support of the Deutsche Forschungsgemeinschaft (DFG; German Research Foundation) under Germany's Excellence Strategy-Cluster of Excellence Matter and Light for Quantum Computing (ML4Q) EXC 2004/1-390534769.

Conflicts of Interest: The authors declare no conflict of Interest.

References

1. Chu, S.; Majumdar, A. Opportunities and Challenges for a Sustainable Energy Future. *Nature* **2012**, *488*, 294–303. [CrossRef] [PubMed]
2. Zou, X.; Zhang, Y. Noble Metal-Free Hydrogen Evolution Catalysts for Water Splitting. *Chem. Soc. Rev.* **2015**, *44*, 5148–5180. [CrossRef] [PubMed]
3. Applications of Capacitors. Available online: https://en.wikipedia.org/wiki/Applications_of_capacitors (accessed on 11 August 2021).
4. Lüker, A. A Short History of Ferroelectricity. Sol-Gel Derived Ferroelectric Thin Films for Voltage Tunable Applications. Ph.D. Thesis, University of Cranfield, Cranfield, UK, 2009.
5. Valasek, J. Piezo-Electric and Allied Phenomena in Rochelle Salt. *Phys. Rev.* **1921**, *17*, 475–481. [CrossRef]
6. Randall, C.A.; Newnham, R.E.; Cross, L.E. History of the First Ferroelectric Oxide, $BaTiO_3$. Available online: https://ceramics.org/ (accessed on 11 August 2021).
7. Schuster, A. Potential Matter—A Holiday Dream. *Nature* **1989**, *58*, 1503. [CrossRef]
8. Barbara, B. Louis Néel: His Multifaceted Seminal Work in Magnetism. *Comptes Rendus Phys.* **2019**, *20*, 631–649. [CrossRef]
9. Kittel, C. Theory of Antiferroelectric Crystals. *Phys. Rev.* **1951**, *82*, 729–732. [CrossRef]
10. Tagantsev, A.K.; Vaideeswaran, K.; Vakhrushev, S.; Filimonov, A.; Burkovsky, R.G.; Shaganov, A.; Andronikova, D.; Rudskoy, A.I.; Baron, A.; Uchiyama, H.; et al. The Origin of Antiferroelectricity in $PbZrO_3$. *Nat. Commun.* **2013**, *4*, 2229. [CrossRef]
11. Hlinka, J.; Ostapchuk, T.; Buixaderas, E.; Kadlec, C.; Kuzel, P.; Gregora, I.; Kroupa, J.; Savinov, M.; Klic, A.; Drahokoupil, J.; et al. Multiple Soft-Mode Vibrations of Lead Zirconate. *Phys. Rev. Lett.* **2014**, *112*, 197601. [CrossRef]
12. Xu, B.; Hellman, O.; Bellaiche, L. Order-Disorder Transition in the Prototypical Antiferroelectric $PbZrO_3$. *Phys. Rev. B* **2019**, *100*, 020102. [CrossRef]
13. Iguez, J.; Stengel, M.; Prosandeev, S.; Bellaiche, L. First-Principles Study of the Multimode Antiferroelectric Transition in $PbZrO_3$. *Phys. Rev. B* **2014**, *90*, 220103. [CrossRef]
14. Zhuo, F.; Li, Q.; Zhou, Y.; Ji, Y.; Yan, Q.; Zhang, Y.; Xi, X.; Chu, X.; Cao, W. Large Field-Induced Strain, Giant Strain Memory Effect, and High Thermal Stability Energy Storage in $(Pb,La)(Zr,Sn,Ti)O_3$ Antiferroelectric Single Crystal. *Acta Mater.* **2018**, *148*, 28–37. [CrossRef]
15. Vales-Castro, P.; Faye, R.; Vellvehi, M.; Nouchokgwe, Y.; Perpiñà, X.; Caicedo, J.M.; Jordà, X.; Roleder, K.; Kajewski, D.; Perez-Tomas, A.; et al. Origin of Large Negative Electrocaloric Effect in Antiferroelectric $PbZrO_3$. *Phys. Rev. B* **2021**, *103*, 054112. [CrossRef]
16. Geng, W.; Liu, Y.; Meng, X.; Bellaiche, L.; Scott, J.F.; Dkhil, B.; Jiang, A. Giant Negative Electrocaloric Effect in Antiferroelectric La-Doped $Pb(ZrTi)O_3$ Thin Films near Room Temperature. *Adv. Mater.* **2015**, *27*, 3165–3169. [CrossRef] [PubMed]
17. Mischenko, A.S.; Zhang, Q.; Scott, J.F.; Whatmore, R.W.; Mathur, N.D. Giant Electrocaloric Effect in Thin-Film $PbZr_{0.95}Ti_{0.05}O_3$. *ChemInform* **2006**, *311*, 1270–1271. [CrossRef]
18. Qiao, L.; Song, C.; Sun, Y.; Fayaz, M.U.; Lu, T.; Yin, S.; Chen, C.; Xu, H.; Ren, T.-L.; Pan, F. Observation of Negative Capacitance in Antiferroelectric $PbZrO_3$ Films. *Nat. Commun.* **2021**, *12*, 4215. [CrossRef] [PubMed]
19. Zhou, Z.; Yang, Q.; Liu, M.; Zhang, Z.; Zhang, X.; Sun, D.; Nan, T.; Sun, N.; Chen, X. Antiferroelectric Materials, Applications and Recent Progress on Multiferroic Heterostructures. *SPIN* **2015**, *05*, 1530001. [CrossRef]
20. Vopson, M.M.; Caruntu, G.; Tan, X. Polarization Reversal and Memory Effect in Anti-Ferroelectric Materials. *Scr. Mater.* **2017**, *128*, 61–64. [CrossRef]
21. Pan, H.; Li, F.; Liu, Y.; Zhang, Q.; Wang, M.; Lan, S.; Zheng, Y.; Ma, J.; Gu, L.; Shen, Y.; et al. Ultrahigh-Energy Density Lead-Free Dielectric Films via Polymorphic Nanodomain Design. *Science* **2019**, *365*, 578–582. [CrossRef] [PubMed]
22. Qi, H.; Zuo, R.; Xie, A.; Tian, A.; Fu, J.; Zhang, Y.; Zhang, S. Ultrahigh Energy-Storage Density in $NaNbO_3$-Based Lead-Free Relaxor Antiferroelectric Ceramics with Nanoscale Domains. *Adv. Funct. Mater.* **2019**, *29*, 1903877. [CrossRef]
23. Pan, H.; Ma, J.; Ma, J.; Zhang, Q.; Liu, X.; Guan, B.; Gu, L.; Zhang, X.; Zhang, Y.-J.; Li, L.; et al. Giant Energy Density and High Efficiency Achieved in Bismuth Ferrite-Based Film Capacitors via Domain Engineering. *Nat. Commun.* **2018**, *9*, 1813. [CrossRef]
24. Veerapandiyan, V.; Benes, F.; Gindel, T.; DeLuca, M. Strategies to Improve the Energy Storage Properties of Perovskite Lead-Free Relaxor Ferroelectrics: A Review. *Materials* **2020**, *13*, 5742. [CrossRef] [PubMed]
25. Mohapatra, P.; Fan, Z.; Cui, J.; Tan, X. Relaxor Antiferroelectric Ceramics with Ultrahigh Efficiency for Energy Storage Applications. *J. Eur. Ceram. Soc.* **2019**, *39*, 4735–4742. [CrossRef]

26. Liu, Z.; Lu, T.; Ye, J.; Wang, G.; Dong, X.; Withers, R.; Liu, Y. Antiferroelectrics for Energy Storage Applications: A Review. *Adv. Mater. Technol.* **2018**, *3*, 1800111. [CrossRef]
27. Li, J.; Li, F.; Xu, Z.; Zhang, S. Multilayer Lead-Free Ceramic Capacitors with Ultrahigh Energy Density and Efficiency. *Adv. Mater.* **2018**, *30*, 1802155. [CrossRef]
28. Hou, C.; Huang, W.; Zhao, W.; Zhang, D.; Yin, Y.; Li, X. Ultrahigh Energy Density in $SrTiO_3$ Film Capacitors. *ACS Appl. Mater. Interfaces* **2017**, *9*, 20484–20490. [CrossRef] [PubMed]
29. Jang, H.W.; Kumar, A.; Denev, S.; Biegalski, M.D.; Maksymovych, P.; Bark, C.W.; Nelson, C.T.; Folkman, C.M.; Baek, S.H.; Balke, N.; et al. Ferroelectricity in Strain-Free $SrTiO_3$ Thin Films. *Phys. Rev. Lett.* **2010**, *104*, 197601. [CrossRef]
30. Li, T.; Deng, S.; Liu, H.; Sun, S.; Li, H.; Hu, S.; Liu, S.; Xing, X.; Chen, J. Strong Room-Temperature Ferroelectricity in Strained $SrTiO_3$ Homoepitaxial Film. *Adv. Mater.* **2021**, *33*, 2008316. [CrossRef]
31. Huang, K.; Ge, G.; Yan, F.; Shen, B.; Zhai, J. Ultralow Electrical Hysteresis along with High Energy-Storage Density in Lead-Based Antiferroelectric Ceramics. *Adv. Electron. Mater.* **2020**, *6*, 1901366. [CrossRef]
32. Wang, H.; Liu, Y.; Yang, T.; Zhang, S. Ultrahigh Energy-Storage Density in Antiferroelectric Ceramics with Field-Induced Multiphase Transitions. *Adv. Funct. Mater.* **2019**, *29*, 1807321. [CrossRef]
33. Palneedi, H.; Peddigari, M.; Hwang, G.-T.; Jeong, D.-Y.; Ryu, J. High-Performance Dielectric Ceramic Films for Energy Storage Capacitors: Progress and Outlook. *Adv. Funct. Mater.* **2018**, *28*, 1803665. [CrossRef]
34. Dong, X.; Li, X.; Chen, X.; Chen, H.; Sun, C.; Shi, J.; Pang, F.; Zhou, H. High Energy Storage Density and Power Density Achieved Simultaneously in $NaNbO_3$-Based Lead-Free Ceramics via Antiferroelectricity Enhancement. *J. Mater.* **2020**, *7*, 629–639. [CrossRef]
35. Zhao, L.; Liu, Q.; Gao, J.; Zhang, S.; Li, J. Lead-Free Antiferroelectric Silver Niobate Tantalate with High Energy Storage Performance. *Adv. Mater.* **2017**, *29*, 1701824. [CrossRef] [PubMed]
36. Li, J.; Shen, Z.; Chen, X.; Yang, S.; Zhou, W.; Wang, M.; Wang, L.; Kou, Q.; Liu, Y.; Li, Q.; et al. Grain-Orientation-Engineered Multilayer Ceramic Capacitors for Energy Storage Applications. *Nat. Mater.* **2020**, *19*, 999–1005. [CrossRef] [PubMed]
37. Peng, B.; Zhang, Q.; Li, X.; Sun, T.; Fan, H.; Ke, S.; Ye, M.; Wang, Y.; Lu, W.; Niu, H.; et al. Giant Electric Energy Density in Epitaxial Lead-Free Thin Films with Coexistence of Ferroelectrics and Antiferroelectrics. *Adv. Electron. Mater.* **2015**, *1*, 1500052. [CrossRef]
38. Pan, H.; Lan, S.; Xu, S.; Zhang, Q.; Yao, H.; Liu, Y.; Meng, F.; Guo, E.-J.; Gu, L.; Yi, D.; et al. Ultrahigh Energy Storage in Superparaelectric Relaxor Ferroelectrics. *Science* **2021**, *374*, 100–104. [CrossRef] [PubMed]
39. Acharya, M.; Banyas, E.; Ramesh, M.; Jiang, Y.; Fernandez, A.; Dasgupta, A.; Ling, H.; Hanrahan, B.; Persson, K.; Neaton, J.B.; et al. Exploring the $Pb_{1-x}Sr_xHfO_3$ System and Potential for High Capacitive Energy Storage Density and Efficiency. *Adv. Mater.* **2021**, *33*, 2105967. [CrossRef]
40. Yang, L.; Kong, X.; Li, F.; Hao, H.; Cheng, Z.; Liu, H.; Li, J.-F.; Zhang, S. Perovskite Lead-Free Dielectrics for Energy Storage Applications. *Prog. Mater. Sci.* **2018**, *102*, 72–108. [CrossRef]
41. Fan, Q.; Ma, C.; Li, Y.; Liang, Z.; Cheng, S.; Guo, M.; Dai, Y.; Ma, C.; Lu, L.; Wang, W.; et al. Realization of High Energy Density in an Ultra-Wide Temperature Range through Engineering of Ferroelectric Sandwich Structures. *Nano Energy* **2019**, *62*, 725–733. [CrossRef]
42. Yang, C.; Lv, P.; Qian, J.; Han, Y.; Ouyang, J.; Lin, X.; Huang, S.; Cheng, Z. Fatigue-Free and Bending-Endurable Flexible Mn-Doped $Na_{0.5}Bi_{0.5}TiO_3$-$BaTiO_3$-$BiFeO_3$ Film Capacitor with an Ultrahigh Energy Storage Performance. *Adv. Energy Mater.* **2019**, *9*, 1803949. [CrossRef]
43. Ma, B.; Hu, Z.; Koritala, R.E.; Lee, T.H.; Dorris, S.E.; Balachandran, U. PLZT Film Capacitors for Power Electronics and Energy Storage Applications. *J. Mater. Sci. Mater. Electron.* **2015**, *26*, 9279–9287. [CrossRef]
44. Jiang, J.; Meng, X.; Li, L.; Guo, S.; Huang, M.; Zhang, J.; Wang, J.; Hao, X.; Zhu, H.; Zhang, S.-T. Ultrahigh Energy Storage Density in Lead-Free Relaxor Antiferroelectric Ceramics via Domain Engineering. *Energy Storage Mater.* **2021**, *43*, 383–390. [CrossRef]
45. Qi, H.; Xie, A.; Tian, A.; Zuo, R. Superior Energy-Storage Capacitors with Simultaneously Giant Energy Density and Efficiency Using Nanodomain Engineered $BiFeO_3$-$BaTiO_3$-$NaNbO_3$ Lead-Free Bulk Ferroelectrics. *Adv. Energy Mater.* **2019**, *10*, 1903338. [CrossRef]
46. Luo, N.; Han, K.; Cabral, M.J.; Liao, X.; Zhang, S.; Liao, C.; Zhang, G.; Chen, X.; Feng, Q.; Li, J.-F.; et al. Constructing Phase Boundary in $AgNbO_3$ Antiferroelectrics: Pathway Simultaneously Achieving High Energy Density and Efficiency. *Nat. Commun.* **2020**, *11*, 4824. [CrossRef] [PubMed]
47. Ge, G.; Huang, K.; Wu, S.; Yan, F.; Li, X.; Shen, B.; Zhai, J. Synergistic Optimization of Antiferroelectric Ceramics with Superior Energy Storage Properties via Phase Structure Engineering. *Energy Storage Mater.* **2020**, *35*, 114–121. [CrossRef]
48. Blue, C.T.; Hicks, J.C.; Park, S.E.; Yoshikawa, S.; Cross, L.E. In Situ X-ray Diffraction Study of the Antiferroelectric-Ferroelectric Phase Transition in PLSnZT. *Appl. Phys. Lett.* **1996**, *68*, 2942–2944. [CrossRef]
49. Cai, Y.; Phillipp, F.; Zimmermann, A.; Zhou, L.; Aldinger, F.; Rühle, M. TEM Study of Superstructure in a Perovskite Lead Lanthanum Zirconate Stannate Titanate Ceramic. *Acta Mater.* **2003**, *51*, 6429–6436. [CrossRef]
50. He, H.; Tan, X. Electric-Field-Induced Transformation of Incommensurate Modulations in Antiferroelectric $Pb_{0.99}Nb_{0.02}[(Zr_{1-x}Sn_x)_{1-y}Ti_y]_{0.98}O_3$. *Phys. Rev. B* **2005**, *72*, 024102. [CrossRef]
51. Li, F.; Lin, D.; Chen, Z.; Cheng, Z.; Wang, J.; Li, C.; Xu, Z.; Huang, Q.; Liao, X.; Chen, L.-Q.; et al. Ultrahigh Piezoelectricity in Ferroelectric Ceramics by Design. *Nat. Mater.* **2018**, *17*, 349–354. [CrossRef]

52. Tan, X.; Ma, C.; Frederick, J.; Beckman, S.; Webber, K.G. The Antiferroelectric ↔ Ferroelectric Phase Transition in Lead-Containing and Lead-Free Perovskite Ceramics. *J. Am. Ceram. Soc.* **2011**, *94*, 4091–4107. [CrossRef]
53. Zhang, T.; Zhao, Y.; Li, W.; Fei, W. High Energy Storage Density at Low Electric Field of ABO_3 Antiferroelectric Films with Ionic Pair Doping. *Energy Storage Mater.* **2018**, *18*, 238–245. [CrossRef]
54. Liu, X.; Li, Y.; Sun, N.; Hao, X. High Energy-Storage Performance of PLZS Antiferroelectric Multilayer Ceramic Capacitors. *Inorg. Chem. Front.* **2019**, *7*, 756–764. [CrossRef]
55. Zhou, H.Y.; Liu, X.Q.; Zhu, X.L.; Chen, X.M. $CaTiO_3$ Linear Dielectric Ceramics with Greatly Enhanced Dielectric Strength and Energy Storage Density. *J. Am. Ceram. Soc.* **2017**, *101*, 1999–2008. [CrossRef]
56. Ravel, B.; Slcron, N.; Yacoby, Y.; Stern, E.A.; Dogan, F.; Rehr, J.J. Order-Disorder Behavior in the Phase Transition of $PbTiO_3$. *Ferroelectrics* **1995**, *164*, 265–277. [CrossRef]
57. Salmani-Rezaie, S.; Ahadi, K.; Strickland, W.M.; Stemmer, S. Order-Disorder Ferroelectric Transition of Strained $SrTiO_3$. *Phys. Rev. Lett.* **2020**, *125*, 087601. [CrossRef]
58. Aksel, E.; Jones, J.L. Advances in Lead-Free Piezoelectric Materials for Sensors and Actuators. *Sensors* **2010**, *10*, 1935–1954. [CrossRef] [PubMed]
59. Whatmore, R.W.; Glazer, A.M. Structural Phase Transitions in Lead Zirconate. *J. Phys. C Solid State Phys.* **1979**, *12*. [CrossRef]
60. Scott, B.A.; Burns, G. Crystal Growth and Observation of the Ferroelectric Phase of $PbZrO_3$. *J. Am. Ceram. Soc.* **1972**, *55*, 331–333. [CrossRef]
61. Kobayashi, K.; Ryu, M.; Doshida, Y.; Mizuno, Y.; Randall, C. Novel High-Temperature Antiferroelectric-Based Dielectric $NaNbO_3$-$NaTaO_3$ Solid Solutions Processed in Low Oxygen Partial Pressures. *J. Am. Ceram. Soc.* **2012**, *96*, 531–537. [CrossRef]
62. Sawaguchi, E. Ferroelectricity versus Antiferroelectricity in the Solid Solutions of $PbZrO_3$ and $PbTiO_3$. *J. Phys. Soc. Jpn.* **1953**, *8*, 615–629. [CrossRef]
63. Chauhan, A.; Patel, S.; Vaish, R.; Bowen, C.R. Anti-Ferroelectric Ceramics for High Energy Density Capacitors. *Materials* **2015**, *8*, 8009–8031. [CrossRef]
64. Chen, D.; Nelson, C.T.; Zhu, X.; Serrao, C.R.; Clarkson, J.D.; Wang, Z.; Gao, Y.; Hsu, S.-L.; Dedon, L.R.; Chen, Z.; et al. A Strain-Driven Antiferroelectric-to-Ferroelectric Phase Transition in La-Doped $BiFeO_3$ Thin Films on Si. *Nano Lett.* **2017**, *17*, 5823–5829. [CrossRef] [PubMed]
65. Borisevich, A.; Eliseev, E.; Morozovska, A.N.; Cheng, C.-J.; Lin, J.-Y.; Chu, Y.-H.; Kan, D.; Takeuchi, I.; Nagarajan, V.; Kalinin, S. Atomic-Scale Evolution of Modulated Phases at the Ferroelectric-Antiferroelectric Morphotropic Phase Boundary Controlled by Flexoelectric Interaction. *Nat. Commun.* **2012**, *3*, 775. [CrossRef] [PubMed]
66. Yamasaki, K.; Soejima, Y.; Fischer, K.F. Superstructure Determination of $PbZrO_3$. *Acta Crystallogr. Sect. B Struct. Sci.* **1998**, *54*, 524–530. [CrossRef]
67. Lu, Z.; Bao, W.; Wang, G.; Sun, S.-K.; Li, L.; Li, J.; Yang, H.; Ji, H.; Feteira, A.; Li, D.; et al. Mechanism of Enhanced Energy Storage Density in $AgNbO_3$-Based Lead-Free Antiferroelectrics. *Nano Energy* **2020**, *79*, 105423. [CrossRef]
68. Xie, A.; Qi, H.; Zuo, R.; Tian, A.; Chen, J.; Zhang, S. An Environmentally-Benign $NaNbO_3$ Based Perovskite Antiferroelectric Alternative to Traditional Lead-Based Counterparts. *J. Mater. Chem. C* **2019**, *7*, 15153–15161. [CrossRef]
69. Xu, X.; Huang, F.-T.; Qi, Y.; Singh, S.; Rabe, K.M.; Obeysekera, D.; Yang, J.; Chu, M.-W.; Cheong, S.-W. Kinetically Stabilized Ferroelectricity in Bulk Single-Crystalline HfO_2:Y. *Nat. Mater.* **2021**, *20*, 826–832. [CrossRef]
70. Silva, J.P.B.; Sekhar, K.C.; Pan, H.; MacManus-Driscoll, J.L.; Pereira, M. Advances in Dielectric Thin Films for Energy Storage Applications, Revealing the Promise of Group IV Binary Oxides. *ACS Energy Lett.* **2021**, *6*, 2208–2217. [CrossRef]
71. Tsai, M.; Zheng, Y.; Lu, S.; Zheng, J.; Pan, H.; Duan, C.; Yu, P.; Huang, R.; Chu, Y. Antiferroelectric Anisotropy of Epitaxial $PbHfO_3$ Films for Flexible Energy Storage. *Adv. Funct. Mater.* **2021**, *31*, 2105060. [CrossRef]
72. Ko, D.-L.; Hsin, T.; Lai, Y.-H.; Ho, S.-Z.; Zheng, Y.; Huang, R.; Pan, H.; Chen, Y.-C.; Chu, Y.-H. High-Stability Transparent Flexible Energy Storage Based on $PbZrO_3$/Muscovite Heterostructure. *Nano Energy* **2021**, *87*, 106149. [CrossRef]
73. Xu, C.; Chen, Y.; Cai, X.; Meingast, A.; Guo, X.; Wang, F.; Lin, Z.; Lo, T.W.; Maunders, C.; Lazar, S.; et al. Two-Dimensional Antiferroelectricity in Nanostripe-Ordered In_2Se_3. *Phys. Rev. Lett.* **2020**, *125*, 047601. [CrossRef]
74. Xu, C.; Mao, J.; Guo, X.; Yan, S.; Chen, Y.; Lo, T.W.; Chen, C.; Lei, D.; Luo, X.; Hao, J.; et al. Two-Dimensional Ferroelasticity in van der Waals Beta′-In_2Se_3. *Nat. Commun.* **2021**, *12*, 3665. [CrossRef] [PubMed]
75. Corker, D.L.; Glazer, A.M.; Dec, J.; Roleder, K.; Whatmore, R. A Re-investigation of the Crystal Structure of the Perovskite $PbZrO_3$ by X-ray and Neutron Diffraction. *Acta Crystallogr. Sect. B Struct. Sci.* **1997**, *53*, 135–142. [CrossRef]
76. Mishra, S.K.; Choudhury, N.; Chaplot, S.L.; Krishna, P.S.R.; Mittal, R. Competing Antiferroelectric and Ferroelectric Interactions in $NaNbO_3$: Neutron Diffraction and Theoretical Studies. *Phys. Rev. B* **2007**, *76*, 024110. [CrossRef]
77. Shimizu, H.; Guo, H.; Reyes-Lillo, S.E.; Mizuno, Y.; Rabe, K.M.; Randall, C.A. Lead-Free Antiferroelectric: $xCaZrO_3$-(1-x)$NaNbO_3$ system ($0 \leq x \leq 0.10$). *Dalton Trans.* **2015**, *44*, 10763. [CrossRef] [PubMed]
78. Kagimura, R.; Singh, D.J. First-Principles Investigations of Elastic Properties and Energetics of Antiferroelectric and Ferroelectric Phases of $PbZrO_3$. *Phys. Rev. B* **2008**, *77*, 104113. [CrossRef]
79. Wei, X.-K.; Tagantsev, A.K.; Kvasov, A.; Roleder, K.; Jia, C.-L.; Setter, N. Ferroelectric Translational Antiphase Boundaries in Nonpolar Materials. *Nat. Commun.* **2014**, *5*, 3031. [CrossRef] [PubMed]
80. Wei, X.-K.; Jia, C.-L.; Roleder, K.; Setter, N. Polarity of Translation Boundaries in Antiferroelectric $PbZrO_3$. *Mater. Res. Bull.* **2015**, *62*, 101–105. [CrossRef]

81. Wei, X.-K.; Vaideeswaran, K.; Sandu, C.S.; Jia, C.-L.; Setter, N. Preferential Creation of Polar Translational Boundaries by Interface Engineering in Antiferroelectric PbZrO3Thin Films. *Adv. Mater. Interfaces* **2015**, *2*, 1500349. [CrossRef]
82. Mani, B.K.; Chang, C.M.; Lisenkov, S.; Ponomareva, I. Critical Thickness for Antiferroelectricity in $PbZrO_3$. *Phys. Rev. Lett.* **2015**, *115*, 097601. [CrossRef] [PubMed]
83. Chaudhuri, A.R.; Arredondo, M.; Hähnel, A.; Morelli, A.; Becker, M.; Alexe, M.; Vrejoiu, I. Epitaxial Strain Stabilization of a Ferroelectric Phase in $PbZrO_3$ Thin films. *Phys. Rev. B* **2011**, *84*, 054112. [CrossRef]
84. MacLaren, I.; Villaurrutia, R.; Schaffer, B.; Houben, L.; Peláiz-Barranco, A. Atomic-Scale Imaging and Quantification of Electrical Polarisation in Incommensurate Antiferroelectric Lanthanum-Doped Lead Zirconate Titanate. *Adv. Funct. Mater.* **2011**, *22*, 261–266. [CrossRef]
85. Fu, Z.; Chen, X.; Li, Z.; Hu, T.; Zhang, L.; Lu, P.; Zhang, S.; Wang, G.; Dong, X.; Xu, F. Unveiling the Ferrielectric Nature of $PbZrO_3$-Based Antiferroelectric Materials. *Nat. Commun.* **2020**, *11*, 3809. [CrossRef]
86. Ma, T.; Fan, Z.; Xu, B.; Kim, T.-H.; Lu, P.; Bellaiche, L.; Kramer, M.J.; Tan, X.; Zhou, L. Uncompensated Polarization in Incommensurate Modulations of Perovskite Antiferroelectrics. *Phys. Rev. Lett.* **2019**, *123*, 217602. [CrossRef]
87. Carpenter, M.A.; Salje, E.K.H.; Graeme-Barber, A. Spontaneous Strain as a Determinant of Thermodynamic Properties for Phase Transitions in Minerals. *Eur. J. Miner.* **1998**, *10*, 621–691. [CrossRef]
88. Puchberger, S.; Soprunyuk, V.; Schranz, W. Diverging Relaxation Times of Domain Wall Motion Indicating Glassy Dynamics in Ferroelastics. *Mater. Res.* **2018**, *21*, e20170842. [CrossRef]
89. Salje, E.K. *Phase Transitions in Ferroelastic and Co-Elastic Crystals*; Cambridge University Press: Cambridge, UK, 1993; ISBN 0521429366.
90. Watanabe, S.; Hidaka, M.; Yoshizawa, H.; Wanklyn, B.M. Antiferroelastic Structural Transitions in $PrAlO_3$ by Means of Neutron Diffraction. *Phys. Status Solidi B* **2005**, *243*, 424–434. [CrossRef]
91. Lines, M.E.; Glass, A.M. *Principles and Applications of Ferroelectrics and Related Materials*; Oxford University Press: Oxford, UK, 1977.
92. Glazer, A.M. The Classification of Tilted Octahedra in Perovskites. *Acta Crystallogr. Sect. B Struct. Crystallogr. Cryst. Chem.* **1972**, *28*, 3384–3392. [CrossRef]
93. Woodward, D.I.; Reaney, I. Electron Diffraction of Tilted Perovskites. *Acta Crystallogr. Sect. B Struct. Sci.* **2005**, *61*, 387–399. [CrossRef]
94. Karpinsky, D.V.; Eliseev, E.; Xue, F.; Silibin, M.V.; Franz, A.; Glinchuk, M.; Troyanchuk, I.O.; Gavrilov, S.; Gopalan, V.; Chen, L.-Q.; et al. Thermodynamic Potential and Phase Diagram for Multiferroic Bismuth Ferrite ($BiFeO_3$). *NPJ Comput. Mater.* **2017**, *3*, 20. [CrossRef]
95. Gu, T.; Scarbrough, T.; Yang, Y.; Íñiguez, J.; Bellaiche, L.; Xiang, H.J. Cooperative Couplings between Octahedral Rotations and Ferroelectricity in Perovskites and Related Materials. *Phys. Rev. Lett.* **2018**, *120*, 197602. [CrossRef]
96. Son, J.Y.; Lee, G.; Jo, M.-H.; Kim, H.; Jang, H.M.; Shin, Y.-H. Heteroepitaxial Ferroelectric $ZnSnO_3$ Thin Film. *J. Am. Chem. Soc.* **2009**, *131*, 8386–8387. [CrossRef] [PubMed]
97. Xu, B.; Iñiguez, J.; Bellaiche, L. Designing Lead-Free Antiferroelectrics for Energy Storage. *Nat. Commun.* **2017**, *8*, 15682. [CrossRef] [PubMed]
98. Kim, J.R.; Jang, J.; Go, K.-J.; Park, S.Y.; Roh, C.J.; Bonini, J.; Kim, J.; Lee, H.G.; Rabe, K.M.; Lee, J.S.; et al. Stabilizing Hidden Room-Temperature Ferroelectricity via a Metastable Atomic Distortion Pattern. *Nat. Commun.* **2020**, *11*, 4944. [CrossRef]
99. Li, Z.; Song, D.; Yu, R.; Ge, B.; Liao, Z.; Li, Y.; Dong, S.; Zhu, J. Competing Interfacial Reconstruction Mechanisms in $La_{0.7}Sr_{0.3}MnO_3/SrTiO_3$ Heterostructures. *ACS Appl. Mater. Interfaces* **2016**, *8*, 24192–24197. [CrossRef]
100. El-Mellouhi, F.; Brothers, E.N.; Lucero, M.J.; Scuseria, G.E. Modeling of the Cubic and Antiferrodistortive Phases of $SrTiO_3$ with Screened Hybrid Density Functional Theory. *Phys. Rev. B* **2011**, *84*, 115122. [CrossRef]
101. Li, Y.L.; Choudhury, S.; Haeni, J.H.; Biegalski, M.D.; Vasudevarao, A.; Sharan, A.; Ma, H.Z.; Levy, J.; Gopalan, V.; Trolier-McKinstry, S.; et al. Phase Transitions and Domain Structures in Strained Pseudocubic (100) $SrTiO_3$ Thin Films. *Phys. Rev. B* **2006**, *73*, 184112. [CrossRef]
102. Nova, T.F.; Disa, A.S.; Fechner, M.; Cavalleri, A. Metastable Ferroelectricity in Optically Strained $SrTiO_3$. *Science* **2019**, *364*, 1075–1079. [CrossRef] [PubMed]
103. Haeni, J.H.; Irvin, P.; Chang, W.; Uecker, R.; Reiche, P.; Li, Y.; Choudhury, S.; Tian, W.; Hawley, M.E.; Craigo, B.; et al. Room-Temperature Ferroelectricity in Strained $SrTiO_3$. *Nature* **2004**, *430*, 758–761. [CrossRef] [PubMed]
104. Xu, R.; Huang, J.; Barnard, E.S.; Hong, S.S.; Singh, P.; Wong, E.K.; Jansen, T.; Harbola, V.; Xiao, J.; Wang, B.Y.; et al. Strain-Induced Room-Temperature Ferroelectricity in $SrTiO_3$ Membranes. *Nat. Commun.* **2020**, *11*, 3141. [CrossRef] [PubMed]
105. Weaver, H. Dielectric Properties of Single Crystals of $SrTiO_3$ at Low Temperatures. *J. Phys. Chem. Solids* **1959**, *11*, 274–277. [CrossRef]
106. Tagantsev, A.K.; Courtens, E.; Arzel, L. Prediction of a Low-Temperature Ferroelectric Instability in Antiphase Domain Boundaries of Strontium Titanate. *Phys. Rev. B* **2001**, *64*, 224107. [CrossRef]
107. Kvasov, A.; Tagantsev, A.K.; Setter, N. Structure and Pressure-Induced Ferroelectric Phase Transition in Antiphase Domain Boundaries of Strontium Titanate from First Principles. *Phys. Rev. B* **2016**, *94*, 054102. [CrossRef]
108. Li, X.; Qiu, T.; Zhang, J.; Baldini, E.; Lu, J.; Rappe, A.M.; Nelson, K.A. Terahertz Field-Induced Ferroelectricity in Quantum Paraelectric $SrTiO_3$. *Science* **2019**, *364*, 1079–1082. [CrossRef]

109. Lee, D.; Lu, H.; Gu, Y.; Choi, S.-Y.; Li, S.-D.; Ryu, S.; Paudel, T.R.; Song, K.; Mikheev, E.; Lee, S.; et al. Emergence of Room-Temperature Ferroelectricity at Reduced Dimensions. *Science* **2015**, *349*, 1314–1317. [CrossRef] [PubMed]
110. Klyukin, K.; Alexandrov, V. Effect of Intrinsic Point Defects on Ferroelectric Polarization Behavior of $SrTiO_3$. *Phys. Rev. B* **2017**, *95*, 035301. [CrossRef]
111. Zhang, X.; Shen, Y.; Xu, B.; Zhang, Q.; Gu, L.; Jiang, J.; Ma, J.; Lin, Y.; Nan, C.-W. Giant Energy Density and Improved Discharge Efficiency of Solution-Processed Polymer Nanocomposites for Dielectric Energy Storage. *Adv. Mater.* **2016**, *28*, 2055–2061. [CrossRef] [PubMed]
112. Kužel, P.; Kadlec, F.; Petzelt, J.; Schubert, J.; Panaitov, G. Highly Tunable $SrTiO_3$/$DyScO_3$ Heterostructures for Applications in the Terahertz Range. *Appl. Phys. Lett.* **2007**, *91*, 232911. [CrossRef]
113. Sluka, T.; Tagantsev, A.K.; Damjanovic, A.; Gureev, M.; Setter, N. Enhanced Electromechanical Response of Ferroelectrics Due to Charged Domain Walls. *Nat. Commun.* **2012**, *3*, 748. [CrossRef]
114. Lisenkov, S.; Yao, Y.; Bassiri-Gharb, N.; Ponomareva, I. Prediction of High-Strain Polar Phases in Antiferroelectric $PbZrO_3$ from a Multiscale Approach. *Phys. Rev. B* **2020**, *102*, 104101. [CrossRef]
115. Ge, J.; Rémiens, D.; Costecalde, J.; Chen, Y.; Dong, X.; Wang, G. Effect of Residual Stress on Energy Storage Property in $PbZrO_3$ Antiferroelectric Thin Films with Different Orientations. *Appl. Phys. Lett.* **2013**, *103*, 162903. [CrossRef]
116. Chandrasekaran, A.; Wei, X.-K.; Feigl, L.; Damjanovic, D.; Setter, N.; Marzari, N. Asymmetric Structure of 90° Domain Walls and Interactions with Defects in $PbTiO_3$. *Phys. Rev. B* **2016**, *93*, 144102. [CrossRef]
117. Wei, X.-K.; Sluka, T.; Fraygola, B.; Feigl, L.; Du, H.; Jin, L.; Jia, C.-L.; Setter, N. Controlled Charging of Ferroelastic Domain Walls in Oxide Ferroelectrics. *ACS Appl. Mater. Interfaces* **2017**, *9*, 6539–6546. [CrossRef]
118. Wei, X.K.; Jia, C.L.; Roleder, K.; Dunin-Borkowski, R.E.; Mayer, J. In Situ Observation of Point-Defect-Induced Unit-Cell-Wise Energy Storage Pathway in Antiferroelectric $PbZrO_3$. *Adv. Funct. Mater.* **2021**, *31*, 2008609. [CrossRef]
119. Zhang, L.; Fu, Z.; Chen, X.; Li, Z.; Hu, T.; Yu, Z.; Wang, G.; Dong, X.; Xu, F. Chemically Tunable Textured Interfacial Defects in $PbZrO_3$-Based Antiferroelectric Perovskite Oxides. *Chem. Mater.* **2021**, *33*, 6743–6751. [CrossRef]
120. Luo, N.; Han, K.; Zhuo, F.; Xu, C.; Zhang, G.; Liu, L.; Chen, X.; Hu, C.; Zhou, H.; Wei, Y. Aliovalent A-Site Engineered $AgNbO_3$ Lead-Free Antiferroelectric Ceramics toward Superior Energy Storage Density. *J. Mater. Chem. A* **2019**, *7*, 14118–14128. [CrossRef]
121. Liu, H.; Fan, L.; Sun, S.; Lin, K.; Ren, Y.; Tan, X.; Xing, X.; Chen, J. Electric-Field-Induced Structure and Domain Texture Evolution in $PbZrO_3$-Based Antiferroelectric by In-Situ High-Energy Synchrotron X-ray Diffraction. *Acta Mater.* **2019**, *184*, 41–49. [CrossRef]
122. Lu, T.; Studer, A.J.; Noren, L.; Hu, W.; Yu, D.; McBride, B.; Feng, Y.; Withers, R.; Chen, H.; Xu, Z.; et al. Electric-Field-Induced AFE-FE Transitions and Associated Strain/Preferred Orientation in Antiferroelectric PLZST. *Sci. Rep.* **2016**, *6*, 23659. [CrossRef] [PubMed]
123. Wang, J.; Liu, Y.; Withers, R.L.; Studer, A.; Li, Q.; Norén, L.; Guo, Y. A Correlated Electron Diffraction, in Situ Neutron Diffraction and Dielectric Properties Investigation of Poled (1-x)$Bi_{0.5}Na_{0.5}TiO_3$-x$BaTiO_3$ Ceramics. *J. Appl. Phys.* **2011**, *110*, 084114. [CrossRef]
124. Ciuchi, I.V.; Chung, C.C.; Fancher, C.M.; Guerrier, J.; Forrester, J.S.; Jones, J.L.; Mitoseriu, L.; Galassi, C. Field-Induced Antiferroelectric to Ferroelectric Transitions in $(Pb_{1-x}La_x)(Zr_{0.90}Ti_{0.10})_{1-x/4}O_3$ investigated by in Situ X-ray Diffraction. *J. Europ. Ceram. Soc.* **2017**, *37*, 4631–4636. [CrossRef]
125. Fan, Z.; Xue, F.; Tutuncu, G.; Chen, L.-Q.; Tan, X. Interaction Dynamics between Ferroelectric and Antiferroelectric Domains in a $PbZrO_3$-Based Ceramic. *Phys. Rev. Appl.* **2019**, *11*, 064050. [CrossRef]
126. Zhang, M.-H.; Zhao, C.; Fulanović, L.; Rödel, J.; Novak, N.; Schökel, A.; Koruza, J. Revealing the Mechanism of Electric-Field-Induced Phase Transition in Antiferroelectric $NaNbO_3$ by in Situ High-Energy X-ray Diffraction. *Appl. Phys. Lett.* **2021**, *118*, 132903. [CrossRef]
127. Wei, X.; Jia, C.; Du, H.; Roleder, K.; Mayer, J.; Dunin-Borkowski, R. An Unconventional Transient Phase with Cycloidal Order of Polarization in Energy-Storage Antiferroelectric $PbZrO_3$. *Adv. Mater.* **2020**, *32*, e1907208. [CrossRef]
128. Jia, C.L.; Lentzen, M.; Urban, K. Atomic-Resolution Imaging of Oxygen in Perovskite Ceramics. *Science* **2003**, *299*, 870–873. [CrossRef] [PubMed]
129. Wei, X.-K.; Jia, C.-L.; Sluka, T.; Wang, B.-X.; Ye, Z.-G.; Setter, N. Néel-like Domain Walls in Ferroelectric Pb(Zr,Ti)O_3 Single Crystals. *Nat. Commun.* **2016**, *7*, 12385. [CrossRef] [PubMed]
130. Urban, K.W.; Jia, C.-L.; Houben, L.; Lentzen, M.; Mi, S.-B.; Tillmann, K. Negative Spherical Aberration Ultrahigh-Resolution Imaging in Corrected Transmission Electron Microscopy. *Philos. Trans. R. Soc. A Math. Phys. Eng. Sci.* **2009**, *367*, 3735–3753. [CrossRef]
131. Findlay, S.; Shibata, N.; Sawada, H.; Okunishi, E.; Kondo, Y.; Ikuhara, Y. Dynamics of Annular Bright Field Imaging in Scanning Transmission Electron Microscopy. *Ultramicroscopy* **2010**, *110*, 903–923. [CrossRef] [PubMed]
132. Lazić, I.; Bosch, E.G.; Lazar, S. Phase contrast STEM for Thin Samples: Integrated Differential Phase Contrast. *Ultramicroscopy* **2016**, *160*, 265–280. [CrossRef] [PubMed]
133. Yücelen, E.; Lazić, I.; Bosch, E.G.T. Phase Contrast Scanning Transmission Electron Microscopy Imaging of Light and Heavy Atoms at the Limit of Contrast and Resolution. *Sci. Rep.* **2018**, *8*, 2676. [CrossRef] [PubMed]
134. Chen, Z.; Jiang, Y.; Shao, Y.-T.; Holtz, M.E.; Odstrčil, M.; Guizar-Sicairos, M.; Hanke, I.; Ganschow, S.; Schlom, D.G.; Muller, D.A. Electron Ptychography Achieves Atomic-Resolution Limits Set by Lattice Vibrations. *Science* **2021**, *372*, 826–831. [CrossRef] [PubMed]

135. Chen, Q.; Dwyer, C.; Sheng, G.; Zhu, C.; Li, X.; Zheng, C.; Zhu, Y. Imaging Beam-Sensitive Materials by Electron Microscopy. *Adv. Mater.* **2020**, *32*, e1907619. [CrossRef]
136. Russo, C.J.; Henderson, R. Charge Accumulation in Electron Cryomicroscopy. *Ultramicroscopy* **2018**, *187*, 43–49. [CrossRef]
137. Yao, L.; Majumdar, S.; Akaslompolo, L.; Inkinen, S.; Qin, Q.H.; van Dijken, S. Electron-Beam-Induced Perovskite-Brownmillerite-Perovskite Structural Phase Transitions in Epitaxial $La_{2/3}Sr_{1/3}MnO_3$ Films. *Adv. Mater.* **2014**, *26*, 2789–2793. [CrossRef]
138. Zheng, H.; Rivest, J.B.; Miller, T.A.; Sadtler, B.; Lindenberg, A.; Toney, M.F.; Wang, L.-W.; Kisielowski, C.; Alivisatos, A.P. Observation of Transient Structural-Transformation Dynamics in a Cu_2S Nanorod. *Science* **2011**, *333*, 206–209. [CrossRef] [PubMed]
139. Liu, H.; Zhou, Z.; Qiu, Y.; Gao, B.; Sun, S.; Lin, K.; Ding, L.; Li, Q.; Cao, Y.; Ren, Y.; et al. An Intriguing Intermediate State as a Bridge between Antiferroelectric and Ferroelectric Perovskites. *Mater. Horiz.* **2020**, *7*, 1912–1918. [CrossRef]
140. Bittner, R.; Humer, K.; Weber, H.W.; Kundzins, K.; Sternberg, A.; Lesnyh, D.A.; Kulikov, D.V.; Trushin, Y.V. Oxygen Vacancy Defects in Antiferroelectric $PbZrO_3$ Thin Film Heterostructures after Neutron Irradiation. *J. Appl. Phys.* **2004**, *96*, 3239–3246. [CrossRef]
141. Gao, R.; Reyes-Lillo, S.E.; Xu, R.; Dasgupta, A.; Dong, Y.; Dedon, L.R.; Kim, J.; Saremi, S.; Chen, Z.; Serrao, C.R.; et al. Ferroelectricity in $Pb_{1+\delta}ZrO_3$ Thin Films. *Chem. Mater.* **2017**, *29*, 6544–6551. [CrossRef]
142. Bednyakov, P.S.; Sturman, B.I.; Sluka, T.; Tagantsev, A.K.; Yudin, P.V. Physics and Applications of Charged Domain Walls. *NPJ Comput. Mater.* **2018**, *4*, 4. [CrossRef]
143. Sluka, T.; Tagantsev, A.K.; Bednyakov, P.; Setter, N. Free-Electron Gas at Charged Domain Walls in Insulating $BaTiO_3$. *Nat. Commun.* **2013**, *4*, 1808. [CrossRef] [PubMed]
144. Hao, X.; Zhai, J.; Zhou, J.; Yue, Z.; Yang, J.; Zhao, W.; An, S. Structure and Electrical Properties of $PbZrO_3$ Antiferroelectric Thin Films Doped with Barium and Strontium. *J. Alloy. Compd.* **2011**, *509*, 271–275. [CrossRef]
145. Zhao, L.; Gao, J.; Liu, Q.; Zhang, S.; Li, J.-F. Silver Niobate Lead-Free Antiferroelectric Ceramics: Enhancing Energy Storage Density by B-Site Doping. *ACS Appl. Mater. Interfaces* **2017**, *10*, 819–826. [CrossRef] [PubMed]
146. Luo, N.; Han, K.; Zhuo, F.; Liu, L.; Chen, X.; Peng, B.; Wang, X.; Feng, Q.; Wei, Y. Design for High Energy Storage Density and Temperature-Insensitive Lead-Free Antiferroelectric Ceramics. *J. Mater. Chem. C* **2019**, *7*, 4999–5008. [CrossRef]
147. Chmaissem, O.; Dabrowski, B.; Kolesnik, S.; Mais, J.; Jorgensen, J.D.; Short, S. Structural and Magnetic Phase Diagrams of $La_{1-x}Sr_xMnO_3$ and $Pr_{1-y}Sr_yMnO_3$. *Phys. Rev. B* **2003**, *67*, 094431. [CrossRef]
148. Terasaki, I.; Ikuta, M.; Yamamoto, T.D.; Taniguchi, H. Impurity-Induced Spin-State Crossover in $La_{0.8}Sr_{0.2}Co_{1-x}Al_xO_3$. *Crystals* **2018**, *8*, 411. [CrossRef]
149. Allen, P.B.; Berger, H.; Chauvet, O.; Forro, L.; Jarlborg, T.; Junod, A.; Revaz, B.; Santi, G. Transport Properties, Thermodynamic Properties, and Electronic Structure of $SrRuO_3$. *Phys. Rev. B* **1996**, *53*, 4393. [CrossRef]
150. Liao, Z.; Li, F.; Gao, P.; Li, L.; Guo, J.; Pan, X.; Jin, R.; Plummer, E.W.; Zhang, J. Origin of the Metal-Insulator Transition in Ultrathin Films of $La_{2/3}Sr_{2/3}MnO_3$. *Phys. Rev. B* **2015**, *92*, 125123. [CrossRef]
151. Yao, L.; Inkinen, S.; van Dijken, S. Direct Observation of Oxygen Vacancy-Driven Structural and Resistive Phase Transitions in $La_{2/3}Sr_{1/3}MnO_3$. *Nat. Commun.* **2017**, *8*, 14544. [CrossRef] [PubMed]
152. Stengel, M.; Spaldin, N.A. Origin of the Dielectric Dead Layer in Nanoscale Capacitors. *Nature* **2006**, *443*, 679–682. [CrossRef]
153. Stengel, M.; Nicola, D.V.; Spaldin, A. Enhancement of Ferroelectricity at Metal-Oxide Interfaces. *Nat. Mater.* **2009**, *8*, 392. [CrossRef]
154. Wei, X.-K.; Yang, Y.; McGilly, L.J.; Feigl, L.; Dunin-Borkowski, R.E.; Jia, C.-L.; Bellaiche, L.; Setter, N. Flexible Polarization Rotation at the Ferroelectric/Metal Interface as a Seed for Domain Nucleation. *Phys. Rev. B* **2018**, *98*, 020102. [CrossRef]
155. Vailionis, A.; Boschker, H.; Siemons, W.; Houwman, E.P.; Blank, D.H.A.; Rijnders, G.; Koster, G. Misfit Strain Accommodation in Epitaxial ABO_3 Perovskites: Lattice Rotations and Lattice Modulations. *Phys. Rev. B* **2011**, *83*, 064101. [CrossRef]
156. Parsons, T.G.; D'Hondt, H.; Hadermann, J.; Hayward, M. Synthesis and Structural Characterization of $La_{1-x}A_xMnO_{2.5}$ (A = Ba, Sr, Ca) Phases: Mapping the Variants of the Brownmillerite Structure. *Chem. Mater.* **2009**, *21*, 5527–5538. [CrossRef]
157. Lee, H.-S.; Park, H.-H. Band Structure Analysis of $La_{0.7}Sr_{0.3}MnO_3$ Perovskite Manganite Using a Synchrotron. *Adv. Condens. Matter Phys.* **2015**, *2015*, 746475. [CrossRef]
158. Nukala, P.; Ahmadi, M.; Wei, Y.; de Graaf, S.; Stylianidis, E.; Chakrabortty, T.; Matzen, S.; Zandbergen, H.W.; Björling, A.; Mannix, D.; et al. Reversible Oxygen Migration and Phase Transitions in Hafnia-Based Ferroelectric Devices. *Science* **2021**, *372*, 630–635. [CrossRef] [PubMed]
159. Bauer, U.; Yao, L.; Tan, A.J.; Agrawal, P.; Emori, S.; Tuller, H.L.; Van Dijken, S.; Beach, G. Magneto-Ionic Control of Interfacial Magnetism. *Nat. Mater.* **2014**, *14*, 174–181. [CrossRef] [PubMed]
160. Li, M.; Pietrowski, M.J.; De Souza, R.A.; Zhang, H.; Reaney, I.; Cook, S.N.; Kilner, J.; Sinclair, D.C. A Family of Oxide Ion Conductors Based on the Ferroelectric Perovskite $Na_{0.5}Bi_{0.5}TiO_3$. *Nat. Mater.* **2013**, *13*, 31–35. [CrossRef] [PubMed]
161. Kim, T.H.; Puggioni, D.; Yuan, Y.; Xie, L.; Zhou, H.; Campbell, N.; Ryan, P.J.; Choi, Y.; Kim, J.-W.; Patzner, J.; et al. Polar Metals by Geometric Design. *Nature* **2016**, *533*, 68–72. [CrossRef]
162. Puggioni, D.; Rondinelli, J.M. Designing a Robustly Metallic Noncenstrosymmetric Ruthenate Oxide with Large Thermopower Anisotropy. *Nat. Commun.* **2014**, *5*, 3432. [CrossRef]
163. Wei, X.; Bihlmayer, G.; Zhou, X.; Feng, W.; Kolen'Ko, Y.V.; Xiong, D.; Liu, L.; Blügel, S.; Dunin-Borkowski, R.E. Discovery of Real-Space Topological Ferroelectricity in Metallic Transition Metal Phosphides. *Adv. Mater.* **2020**, *32*, e2003479. [CrossRef]

164. Ali, F.; Liu, X.; Zhou, D.; Yang, X.; Xu, J.; Schenk, T.; Müller, J.; Schroeder, U.; Cao, F.; Dong, X. Silicon-Doped Hafnium Oxide Anti-Ferroelectric Thin Films for Energy Storage. *J. Appl. Phys.* **2017**, *122*, 144105. [CrossRef]
165. Park, M.H.; Kim, H.J.; Kim, Y.J.; Moon, T.; Kim, K.D.; Hwang, C.S. Thin $Hf_xZr_{1-x}O_2$ Films: A New Lead-Free System for Electrostatic Supercapacitors with Large Energy Storage Density and Robust Thermal Stability. *Adv. Energy Mater.* **2014**, *4*, 1400610. [CrossRef]
166. Yuan, Q.; Yao, F.-Z.; Cheng, S.-D.; Wang, L.; Wang, Y.; Mi, S.-B.; Wang, Q.; Wang, X.; Wang, H. Bioinspired Hierarchically Structured All-Inorganic Nanocomposites with Significantly Improved Capacitive Performance. *Adv. Funct. Mater.* **2020**, *30*. [CrossRef]
167. Wei, X.-K.; Prokhorenko, S.; Wang, B.-X.; Liu, Z.; Xie, Y.-J.; Nahas, Y.; Jia, C.-L.; Dunin-Borkowski, R.E.; Mayer, J.; Bellaiche, L.; et al. Ferroelectric Phase-Transition Frustration near a Tricritical Composition Point. *Nat. Commun.* **2021**, *12*, 5322. [CrossRef] [PubMed]